Electronic Supplementary Material (ESI) for ChemComm.


**Supporting Information for:**

# Impact of Partial Interpenetration in a Hybrid Ultramicroporous Material on $C_2H_2/C_2H_4$ Separation Performance

**Materials and Methods**

All starting reagents were purchased from commercial sources and used as received without further purification. Solvents used were fresh and stored over molecular sieves.

**Synthesis of [Cu(1,2-bis(4-pyridyl)diazene)$_2$(SiF)$_6$]$_n$ SIFSIX-14-Cu-i, 99% 2-Fold Interpenetrated (1).** Copper (II) hexafluorosilicate (123.6 mg, 0.6 mmol) and 4,4'-azopyridine (220.8mg, 1.2 mmol) were immersed in 30 ml of methanol in a 250 ml Parr® teflon bomb. The vessel was placed in a laboratory oven at 120 °C for 1 h forming a saffron micro-crystalline powder. (CAUTION! Do not seal bottle tightly as the evaporating methanol could pressurize the bottle leading to the glass breaking). The reaction vessel was removed from the oven and allowed to stand and cool to ambient temperature. The precipitate was collected with a Pasteur pipette and continuously washed with dried methanol until the solvent ran clear. The material was submerged in a scintillation vial of dried methanol. In our hands, the material remains stable in this condition.

**Synthesis of [Cu(1,2-bis(4-pyridyl)diazene)$_2$(SiF)$_6$]$_n$ SIFSIX-14-Cu-i, 93% 2-Fold Interpenetrated (2).** This reaction was carried out identically to that previously reported.[1] In a 500 ml Schott Duran® bottle, copper (II) hexafluorosilicate (123.6 mg, 0.6 mmol) and 4,4'-azopyridine (123.6 mg, 0.6 mmol) were immersed in 30 ml of methanol. The loosely capped bottle was placed in a laboratory oven at 120 °C for 1 h forming a saffron micro-crystalline powder. (CAUTION! Do not seal bottle tightly as the evaporating methanol could pressurize the bottle leading to the glass breaking). Upon removal from the oven, the reaction vessel and ca. 15 ml of methanol was added and the precipitate collected with a Pasteur pipette. The sample was continuously washed with

dried methanol until the solvent ran clear. The material was submerged in a scintillation vial of dried methanol. In our hands, the material remains stable in this condition.

**Synthesis of $[Cu(1,2\text{-bis}(4\text{-pyridyl})diazene)_2(SiF)_6]_n$ SIFSIX-14-Cu-i, 89% 2-Fold Interpenetrated (3).** In a 500 ml Schott Duran® bottle, copper (II) hexafluorosilicate (123.6 mg, 0.6 mmol) and 4,4'-azopyridine (123.6 mg, 0.6 mmol) were immersed in 30 ml of methanol. The loosely capped bottle was placed in a laboratory oven at 120 °C for 1 day forming a saffron micro-crystalline powder. (CAUTION! Do not seal bottle tightly as the evaporating methanol could pressurize the bottle leading to the glass breaking). Upon removal from the oven, the reaction vessel and ca. 15 ml of methanol was added and the precipitate collected with a Pasteur pipette. The sample was continuously washed with dried methanol until the solvent ran clear. The material was submerged in a scintillation vial of dried methanol. In our hands, the material remains stable in this condition.

**Synthesis of $[Cu(1,2\text{-bis}(4\text{-pyridyl})diazene)_2(SiF)_6]_n$ SIFSIX-14-Cu-i, 70% 2-Fold Interpenetrated (4).** In a 500 ml Schott Duran® bottle, copper (II) hexafluorosilicate (123.6 mg, 0.6 mmol) and 4,4'-azopyridine (123.6 mg, 0.6 mmol) were immersed in 30 ml of methanol. The loosely capped bottle was placed in a laboratory oven at 120 °C for 1 week forming a saffron micro-crystalline powder. (CAUTION! Do not seal bottle tightly as the evaporating methanol could pressurize the bottle leading to the glass breaking). Upon removal from the oven, the reaction vessel and ca. 15 ml of methanol was added and the precipitate collected with a Pasteur pipette. The sample was continuously washed with dried methanol until the solvent ran clear. The material was submerged in a scintillation vial of dried methanol. In our hands, the material remains stable in this condition.

**Powder X-ray Diffraction Studies**

**Laboratory X-ray Powder Diffraction.** A Panalytical Empyrean diffractometer was used in Bragg-Brentano geometry (40 kV, 40 mA, $CuK_{\alpha 1,2}$ ($\lambda$ = 1.5418 Å). A 0.5 s/step scan speed was used with a step size of 0.05° in 2θ (6°/min) at room temperature, 4° < 2θ < 40° (Figure S3.1 – S3.5).

**Synchrotron X-ray Powder Diffraction.** In order to obtain high quality diffraction data required for quantitative refinement studies, synchrotron X-ray diffraction studies were carried out at beamline i-11 of the Diamond light source ($\lambda$ = 0.82529(2) Å; Zero point = -0.006864(3)°). Wet samples were loaded into 0.6 mm quartz capillary tubes and sealed. A 2 s scan was used with the positional scanning detector (Figure S3.6 – S3.10).

**Quantitative Refinement.** Analyses of the partial interpenetration observed in **SIFSIX-14-Cu-i** were carried out in GSAS-II. Peaks were fitted and lattice parameters were determined for both *P*4/*mmm* and *I*4/*mmm* settings. Each phase and its weight fraction was refined through whole powder pattern decomposition using the Le Bail method (Table S3.1).

The weight fraction of each phase was then cross-validated with 77 K $N_2$ adsorption data and molecular modelling data. That one could consider that N2 adsorption varies with respect to the fractional concentration of ultramicropores (interpenetrated) and micropores (non-interpenetrated), then the observed adsorption data for partially interpenetrated samples must therefore be approximately the sum of both fractional concentrations such that the linear Diophantine equation (1) could be satistified:

$$ax + by = c \qquad (1)$$

Where *a* and *b* are the uptake values for interpenetrated and non-interpenetrated compounds (643.5 $cm^3/g$ for non-interpenetrated; assumed to be zero for interpenetrated), respectively. The observed 77 K $N_2$ data for each compound is represented in the equation by *c* (Table S3.1).

**Gas Sorption Studies**

Low pressure gas adsorption studies were carried out (to 1 bar) on a Micromeritics TriStart II PLUS (77 K $N_2$ sorption studies) and a Micromeritics 3-Flex (298 K $C_2H_2$ and $C_2H_4$) porosimeter. Each sample was degassed overnight at room temperature using a SmartVacPrep instrument. A Julabo ME (v.2) recirculating control system (ethylene glycol/water mixture) was used to control 298 K experiments. The temperature of 77 K $N_2$ experiments were maintained using a 4 L Dewar flask filled with liquid $N_2$ (Figure S3.11 – S3.14).

**Ideal Adsorbed Solution Theory.** Selectivity of one gas over another in a gas mixture was calculated using the ideal adsorbed solution theory (IAST) as implemented in the program pyIAST.[2-4] In this study, we calculated the selectivity of $C_2H_2$ over $C_2H_4$ in 1:99 $C_2H_2/C_2H_4$ gas mixture (Table S2; Figures S3.15 – S3.18).

Experimental isotherms were fitted with adsorption models, $n_i^{\circ}(P)$, that provided the best root mean square error (RMSE) and observable fitting. The Dual-Site Langmuir Isotherm Model (eq. 2) was used for all $C_2H_2$ adsorption data and the Henry Isotherm Model (eq. 3) was used for $C_2H_4$ adsorption isotherms.

Dual-Site Langmuir Isotherm Model

$$n_i^{\circ}(P) = M_1 \frac{K_1 P}{1 + K_1 P} + M_2 \frac{K_2 P}{1 + K_2 P} \qquad (2)$$

Where $(P)$ is pressure, $M_i$ is the number of adsorption sites of type $i$ that has constants $K_i$ (units: pressure$^{-1}$) for sites 1 and 2.

Henry Isotherm Model

$$n_i^{\circ}(P) = K_H P \qquad (3)$$

Where $(P)$ is pressure and $K_H$ is the Henry coefficient (units: loading/pressure).

**Thermal Studies**

**Thermogravimetric analysis (TGA).** All samples were heated under an $N_2$ atmosphere from room temperature to 400 °C in a TA instruments Q50 thermal analyzer (Figures S3.19 – S3.22).

**Differential Scanning Calorimetry (DSC).** Each sample was added, while wet, to a hermetically sealed pan and a pinhole added to the seal to allow for solvent evaporation upon heating. Each sample was studied using a TA instruments Q2000 differential scanning calorimeter. Samples were heated from room temperature to 120 °C at a rate of 20 °C/min and then held for 5 min to ensure complete evolution of trapped solvent. The samples were then heated to 350 °C at a rate of 20 °C/min to observe the degradation profile and then cooled back to 35 °C at a rate of 20 °C/min (Figures S3.23 – S3.27).

## Infrared Spectroscopy

Samples were mounted onto a Perkin Elmer Spectrum 100 Fourier-transform infrared-spectrometer (FT-IR) with Universal ATR and data was collected between 4000 $cm^{-1}$ and 400 $cm^{-1}$ (Figures S3.28 – S3.32).

## Dynamic Breakthrough Measurements

Activated samples were placed in a quartz tube (Ø = 8 mm) to form a fixed bed held in place using quartz wool. Each sample was kept under a dry helium flow to remove atmospheric contaminants. A $C_2H_2/C_2H_4$ mixture (1/99, *v/v*) was passed over the packed bed with a total flow rate of 5 ml/min at 298 K. The outlet gas concentration was continuously monitored using a Hiden HPR-20 QIC evolved gas analysis mass spectrometer (EGA-MS) (Figures S3.33 – S3.37).

## Stability Testing

In order to test the stability of each compound, samples were dried on filter paper and kept exposed to ambient temperature/pressure/humidity for 24 h, wherein powder X-ray diffraction studies indicated each compound had transformed to the **sql-c*** network topology, as previously reported[1] (Figures S3.38).

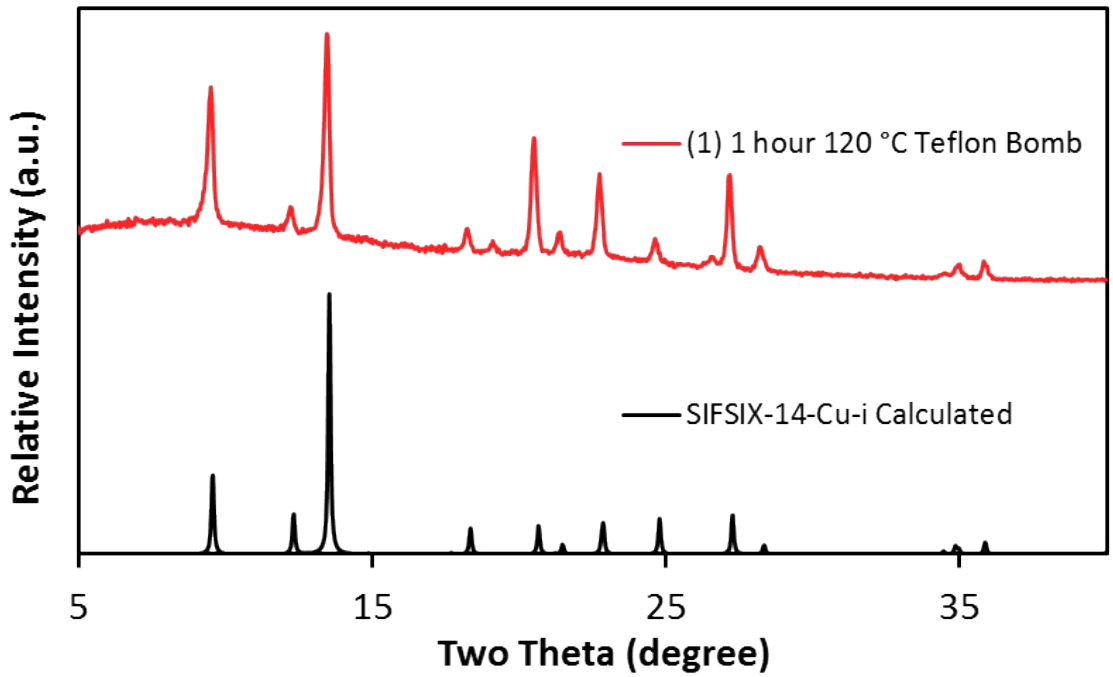


**Figure S3.1.** Laboratory X-ray powder diffractogram of the **SIFSIX-14-Cu-i** sample obtained from a Parr® teflon bomb after heating at 120 °C for 1 hour.

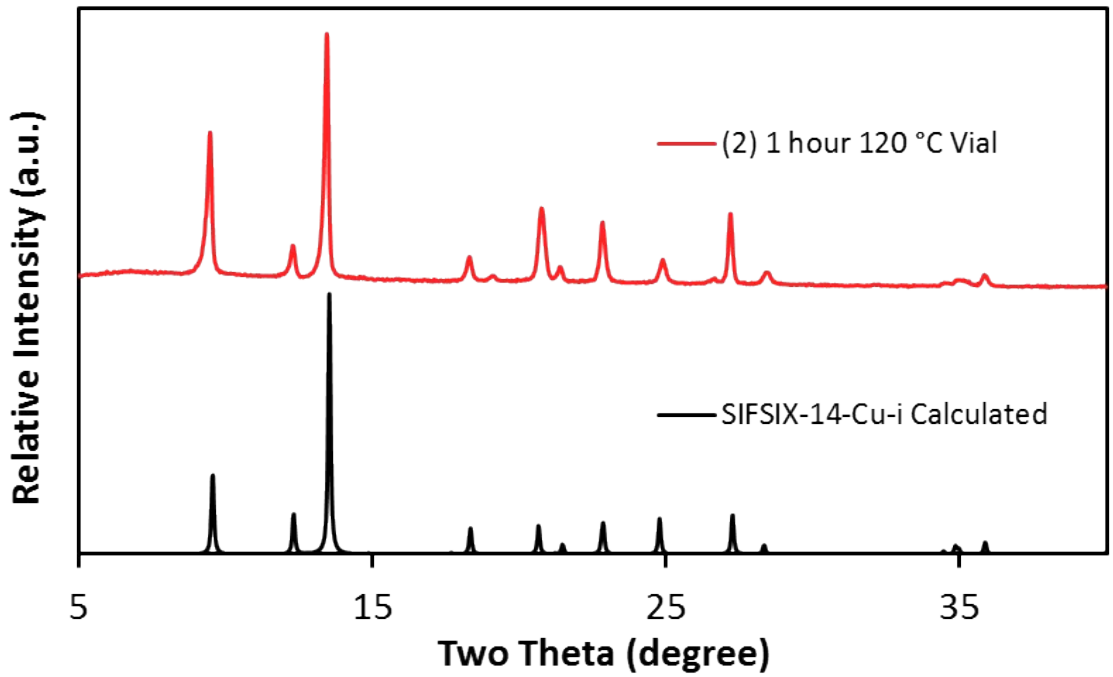


**Figure S3.2.** Laboratory X-ray powder diffractogram of the **SIFSIX-14-Cu-i** sample obtained from a Schott® bottle after heating at 120 °C for 1 hour.

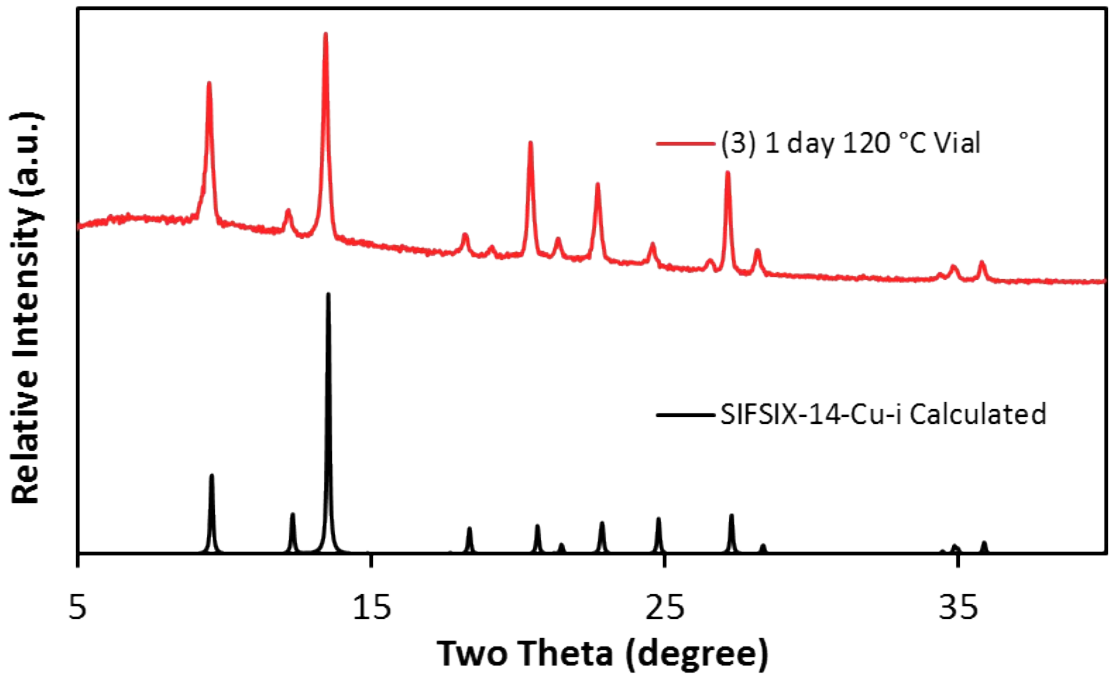


**Figure S3.3.** Laboratory X-ray powder diffractogram of the **SIFSIX-14-Cu-i** sample obtained from a Schott® bottle after heating at 120 °C for 1 day.

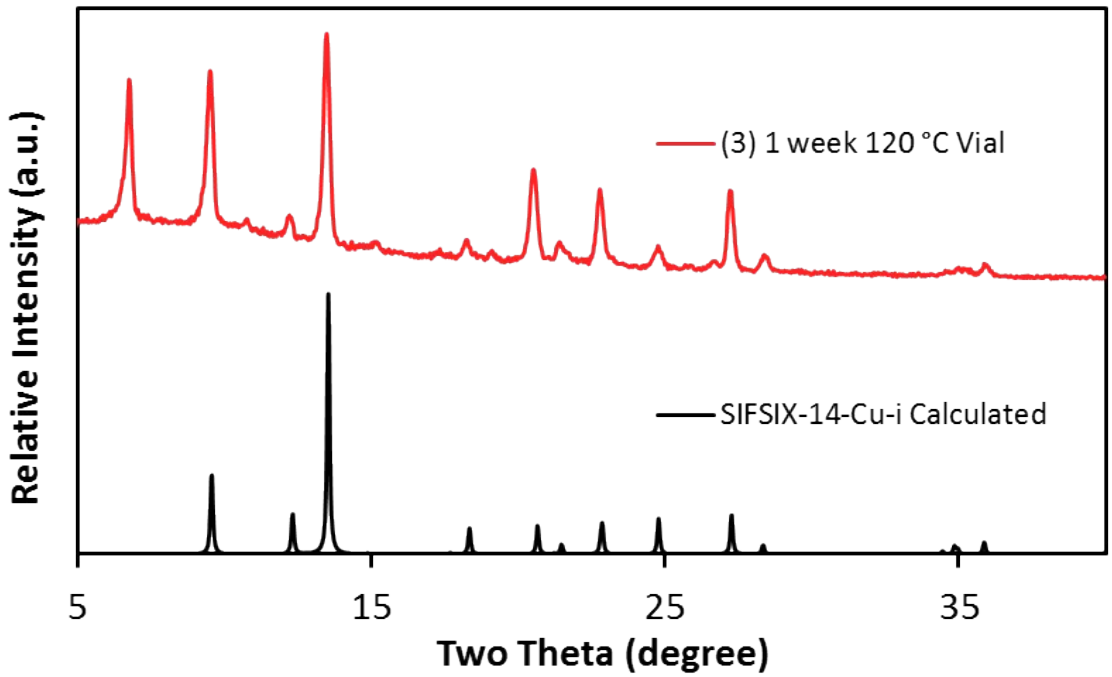


**Figure S3.4.** Laboratory X-ray powder diffractogram of the **SIFSIX-14-Cu-i** sample obtained from a Schott® bottle after heating at 120 °C for 1 week.

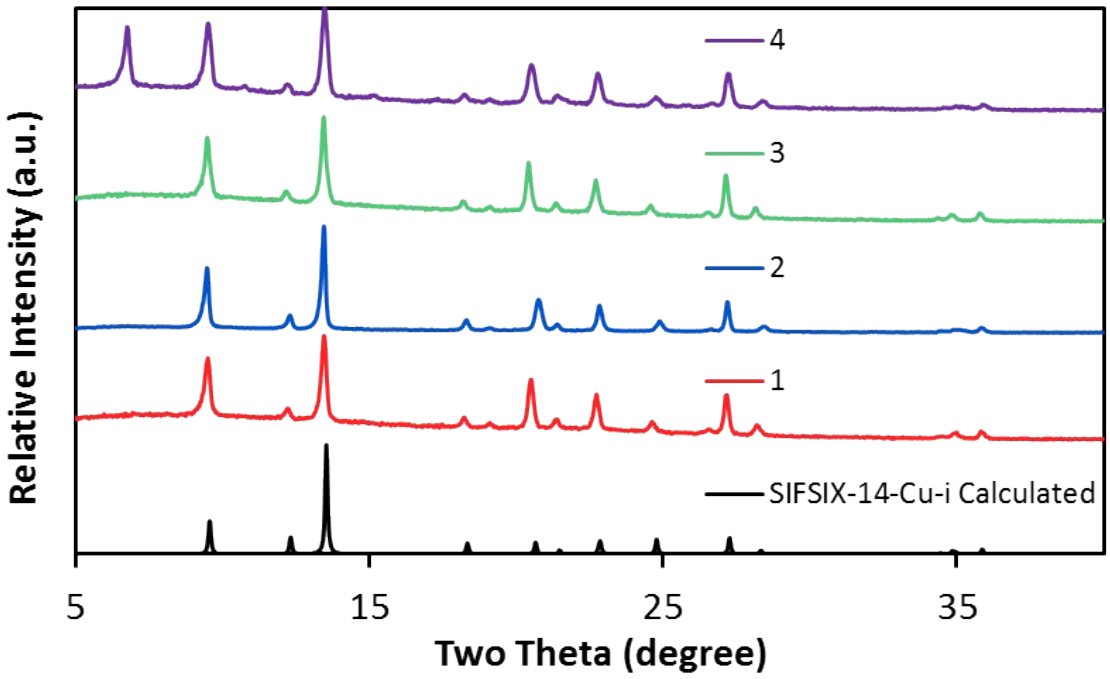


**Figure S3.5.** Laboratory X-ray powder diffractograms of all compounds reported herein.

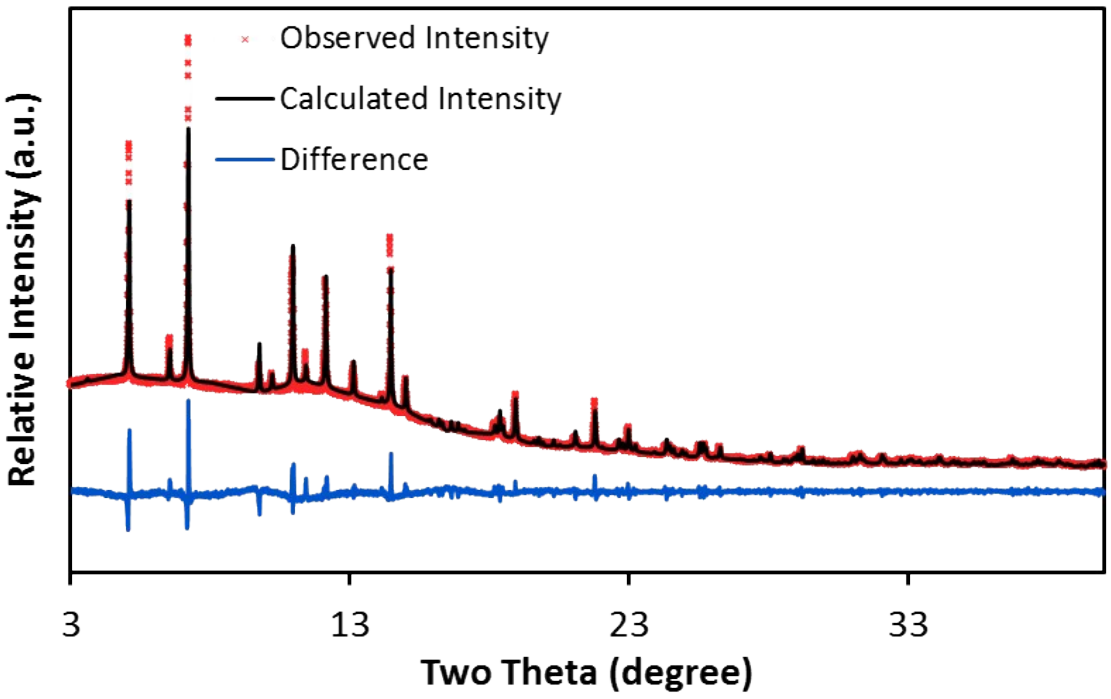


**Figure S3.6.** Synchrotron X-ray powder diffractogram of the **SIFSIX-14-Cu-i** sample obtained from a Parr® teflon bomb after heating at 120 °C for 1 hour.

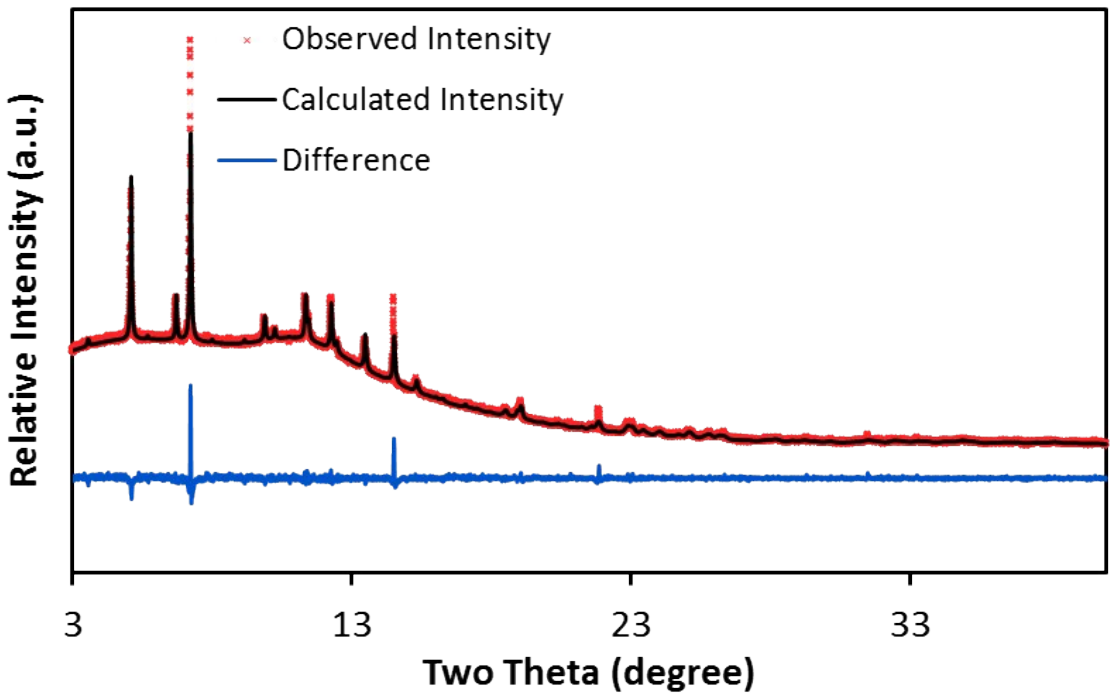


**Figure S3.7.** Synchrotron X-ray powder diffractogram of the **SIFSIX-14-Cu-i** sample obtained from a Schott® bottle after heating at 120 °C for 1 hour.

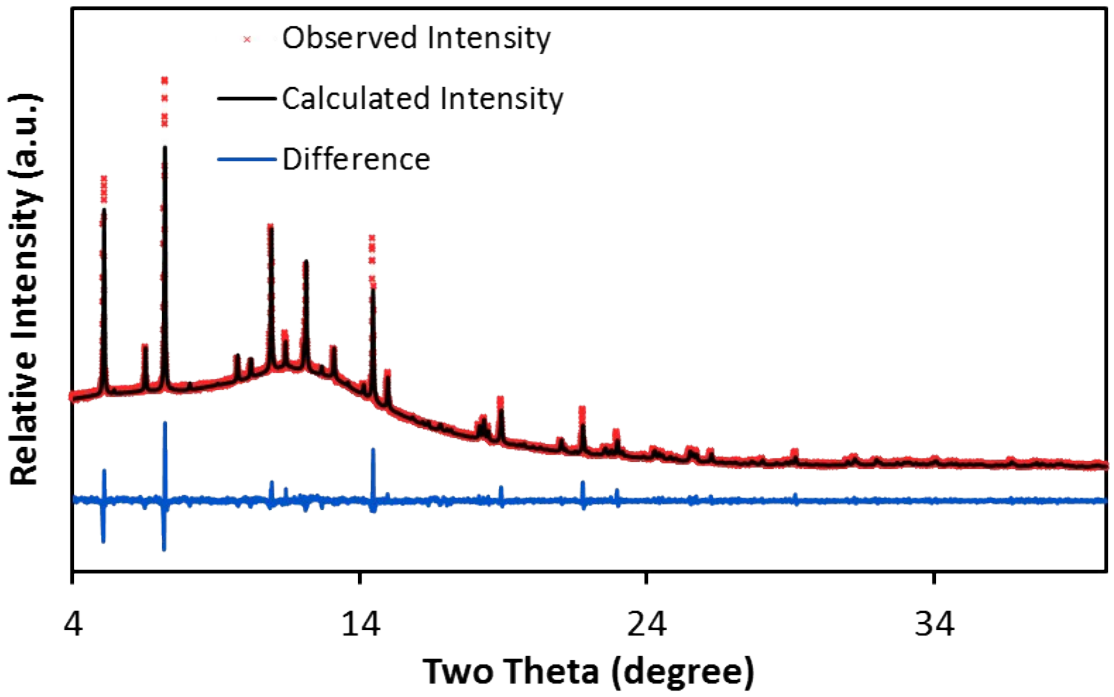


**Figure S3.8.** Synchrotron X-ray powder diffractogram of the **SIFSIX-14-Cu-i** sample obtained from a Schott® bottle after heating at 120 °C for 1 day.

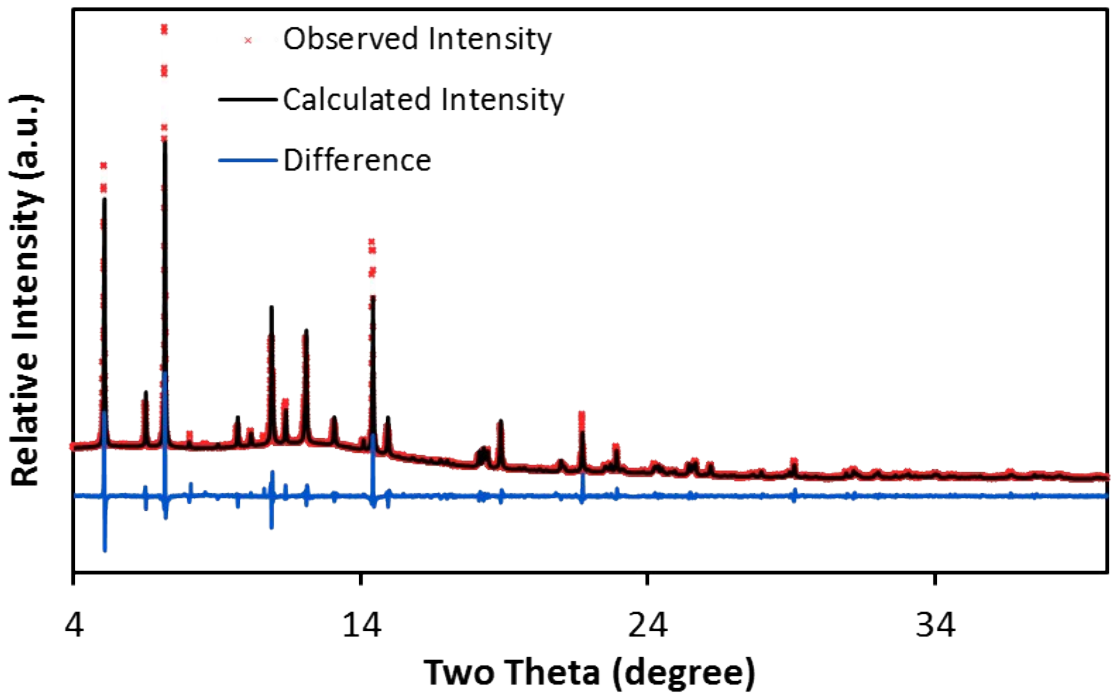


**Figure S3.9.** Synchrotron X-ray powder diffractogram of the **SIFSIX-14-Cu-i** sample obtained from a Schott® bottle after heating at 120 °C for 1 week.

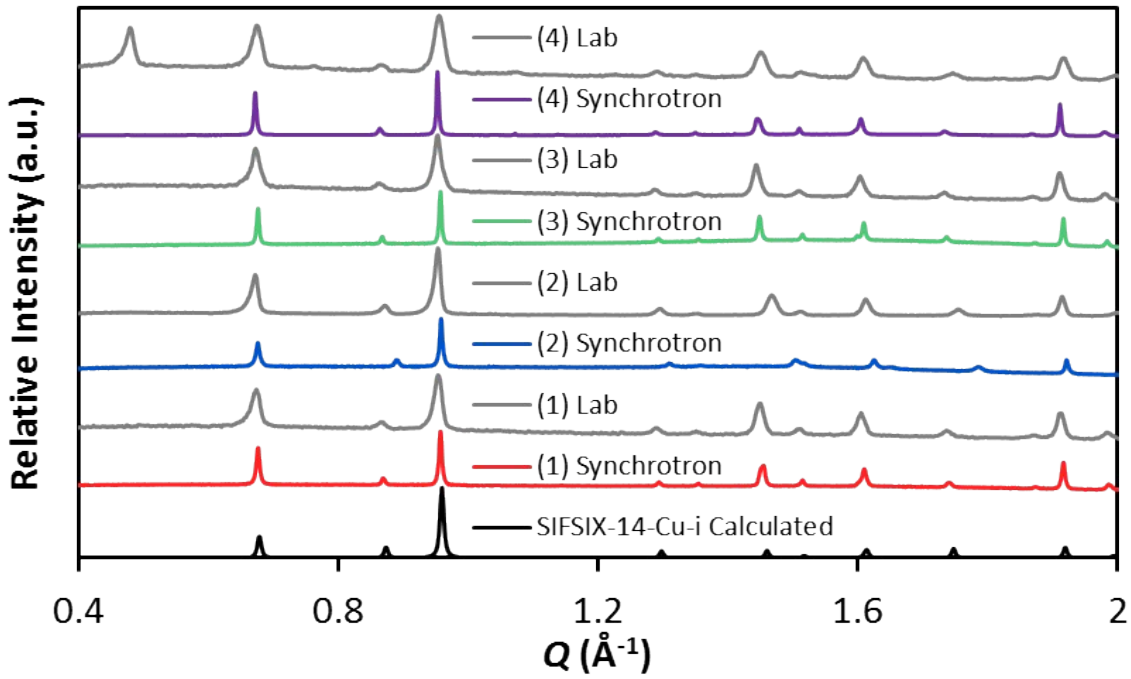


**Figure S3.10.** Synchrotron and Laboratory X-ray powder diffractograms of all compounds reported herein (Q spacing).

**Table S3.1. Quantitative phase analysis data.**

| | | Compounds | | | |
|---|---|---|---|---|---|
| **Crystallographic Data** | **Phase 1** (*I*4/*mmm*) | **1** | **2** | **3** | **4** |
| | *a* (Å) | 13.09286 | 13.05278 | 13.09573 | 13.13327 |
| | *c* (Å) | 8.63163 | 8.332017 | 8.65585 | 8.68294 |
| | $RF^2$ | 0.0765 | 0.02716 | 0.01171 | 0.01453 |
| | **Phase 2** (*P*4/*mmm*) | **1** | **2** | **3** | **4** |
| | *a* (Å) | 13.06307 | 13.19122 | 13.07570 | 13.16352 |
| | *c* (Å) | 8.76253 | 8.27659 | 8.67638 | 8.64724 |
| | $RF^2$ | 0.02779 | 0.07407 | 0.02540 | 0.02369 |
| | **Total** | **1** | **2** | **3** | **4** |
| | $R_p$ | 0.0325 | 0.01549 | 0.0176 | 0.0262 |
| | $wR_p$ | 0.04567 | 0.02444 | 0.03042 | 0.04885 |
| | $wR_{exp}$ | 0.0162 | 0.01577 | 0.0142 | 0.094 |
| | GOOF | 2.83 | 1.55 | 2.14 | 5.17 |
| | **Wt. Fraction (Phase 1)** | **0.995** | **0.943** | **0.893** | **0.697** |
| | **Wt. Fraction (Phase 2)** | **0.005** | **0.058** | **0.107** | **0.303** |
| **Gas Sorption Data** | $N_2$ Uptake (5 mmHg) | 6.273184502 | 46.01749329 | 68.77180474 | 159.5860954 |
| | (Phase 1) | 0.9903 | 0.9285 | 0.8931 | 0.7520 |
| | (Phase 2) | 0.0097 | 0.0715 | 0.1069 | 0.2480 |
| | $N_2$ Uptake (70 mmHg) | 8.068504859 | 50.13816934 | 73.82417221 | 186.0047739 |
| | (Phase 1) | 0.9875 | 0.9221 | 0.8853 | 0.7110 |
| | (Phase 2) | 0.0125 | 0.0779 | 0.1147 | 0.2890 |
| | $N_2$ Uptake (140 mmHg) | 8.847279729 | 50.42165614 | 75.53513971 | 191.3960483 |
| | (Phase 1) | 0.9863 | 0.9216 | 0.8826 | 0.7026 |
| | (Phase 2) | 0.0137 | 0.0784 | 0.1174 | 0.2974 |
| | $N_2$ Uptake (180 mmHg) | 9.182487232 | 50.35656918 | 76.23631162 | 193.6488442 |
| | (Phase 1) | 0.9857 | 0.9217 | 0.8815 | 0.6991 |
| | (Phase 2) | 0.0143 | 0.0783 | 0.1185 | 0.3009 |
| | $N_2$ Uptake (735 mmHg) | 23.55228009 | 68.92747552 | 96.6078192 | 252.6777112 |
| | (Phase 1) | 0.9634 | 0.8929 | 0.8499 | 0.6073 |
| | (Phase 2) | 0.0366 | 0.1071 | 0.1501 | 0.3927 |
| | **Wt. Fraction (Phase 1)** | **0.9826** | **0.9174** | **0.8785** | **0.6944** |
| | **Wt. Fraction (Phase 2)** | **0.01738** | **0.08263** | **0.12151** | **0.30561** |
| | **Ave. Wt. Fraction (Phase 1)** | **0.99** | **0.93** | **0.89** | **0.70** |
| | **Ave. Wt. Fraction (Phase 2)** | **0.01** | **0.07** | **0.11** | **0.30** |

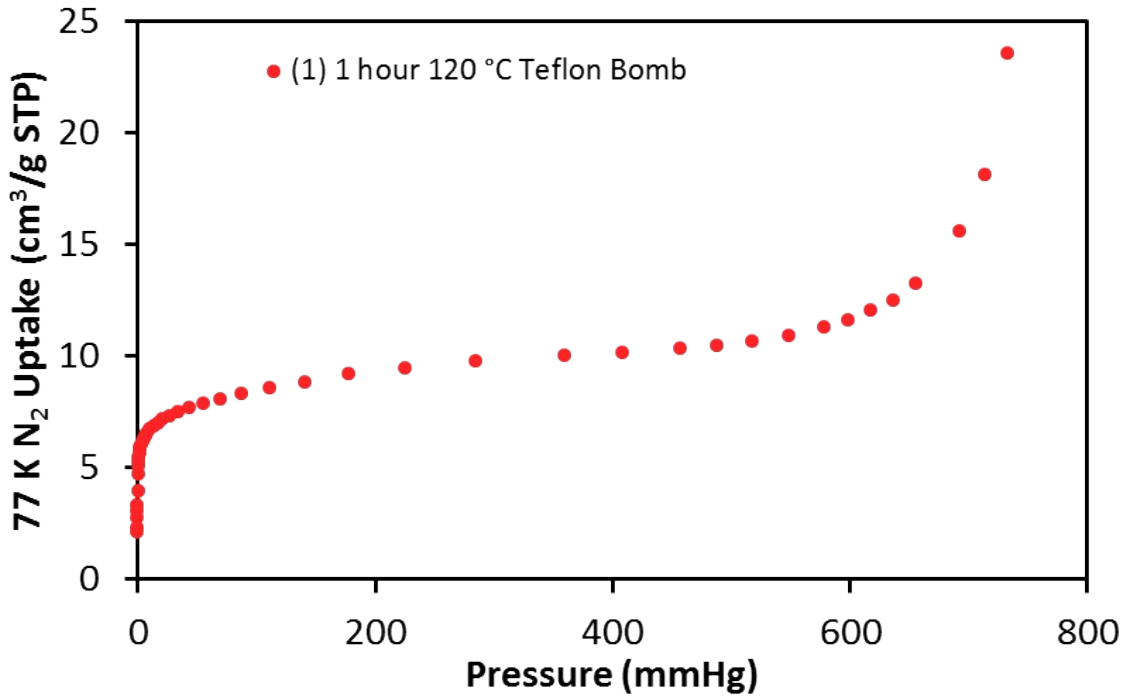


**Figure S3.11.** 77 K $N_2$ adsorption isotherm for the **SIFSIX-14-Cu-i** sample obtained from a Parr® teflon bomb after heating at 120 °C for 1 hour.

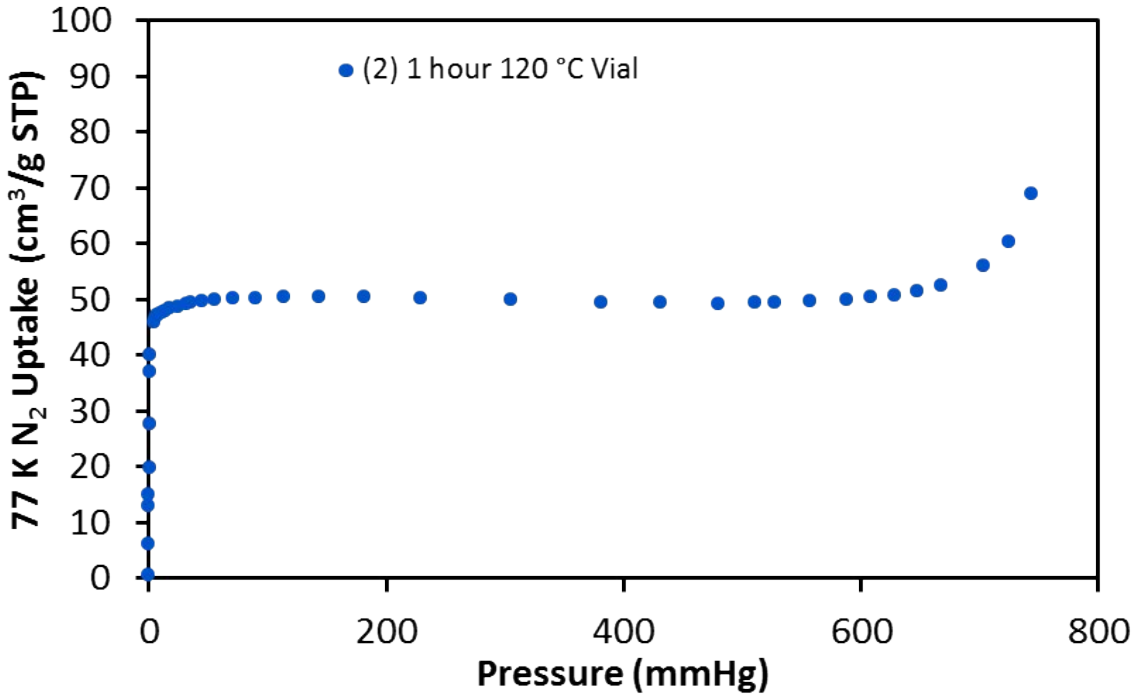


**Figure S3.12.** 77 K $N_2$ adsorption isotherm for the **SIFSIX-14-Cu-i** sample obtained from a Schott® bottle after heating at 120 °C for 1 hour.

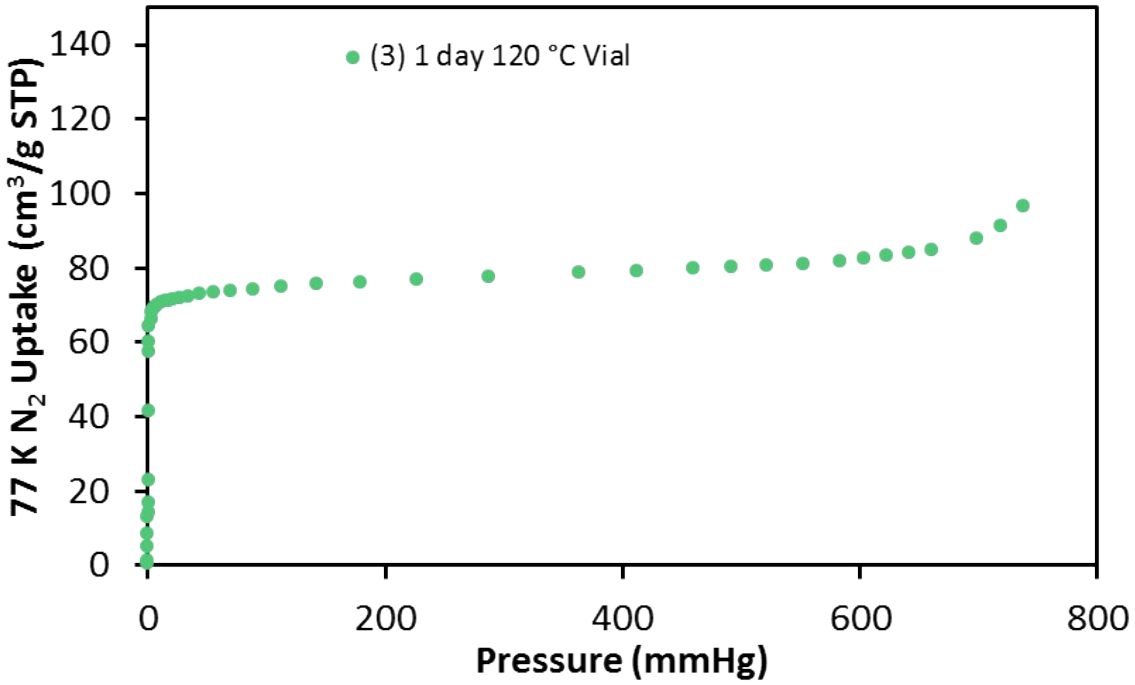


**Figure S3.13.** 77 K $N_2$ adsorption isotherm for the **SIFSIX-14-Cu-i** sample obtained from a Schott® bottle after heating at 120 °C for 1 day.

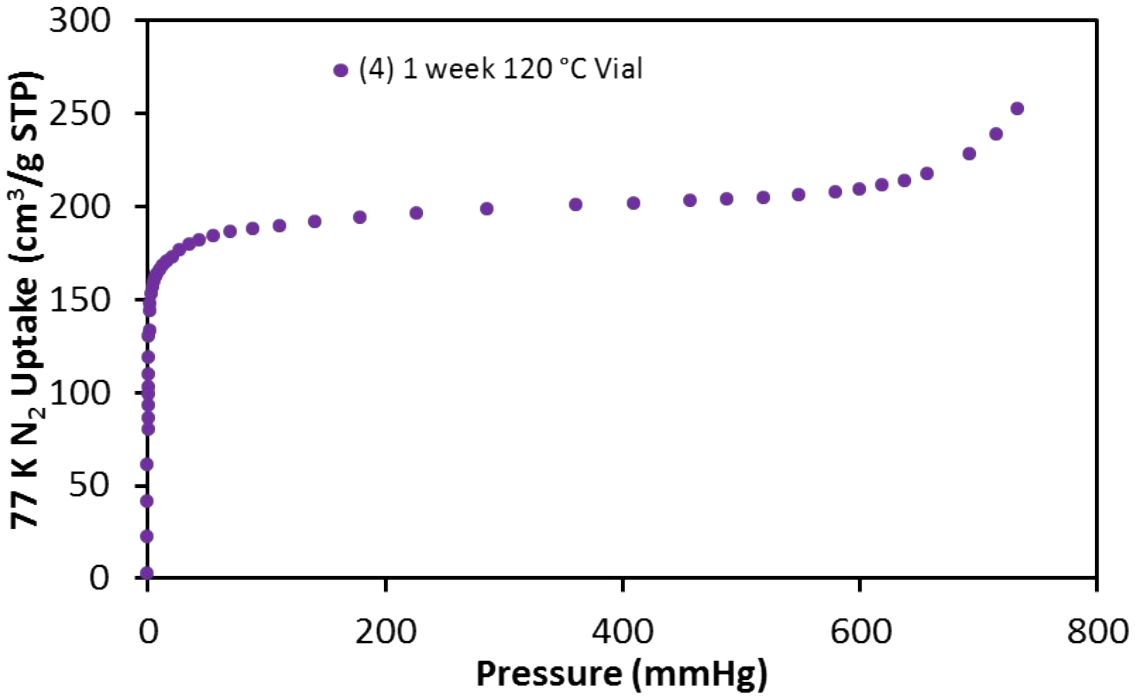


**Figure S3.14.** 77 K $N_2$ adsorption isotherm for the **SIFSIX-14-Cu-i** sample obtained from a Schott® bottle after heating at 120 °C for 1 week.

**Table S2.** Isotherm fitting data

| **$C_2H_2$** | **1** | **2** | **3** | **4** |
|---|---|---|---|---|
| Isotherm | | | | |
| Model | *Dual-Site Langmuir* | | | |
| M1 | 2.799174 | 2.387423 | 2.856387 | 3.330419 |
| K1 | 0.014613 | 0.012506 | 0.013560 | 0.014488 |
| M2 | 2.949824 | 2.484766 | 2.651546 | 2.449717 |
| K2 | 1.600007 | 2.298191 | 2.166130 | 2.215117 |
| RMSE | 0.0387149841571 | 0.0836280201511 | 0.0542084111698 | 0.0499177844741 |
| **$C_2H_4$** | **1** | **2** | **3** | **4** |
| Isotherm | | | | |
| Model | *Henry* | | | |
| KH | 0.007981 | 0.007712 | 0.009058 | 0.011363 |
| RMSE | 0.0180316346498 | 0.0641944942838 | 0.0513209830147 | 0.0407525529006 |

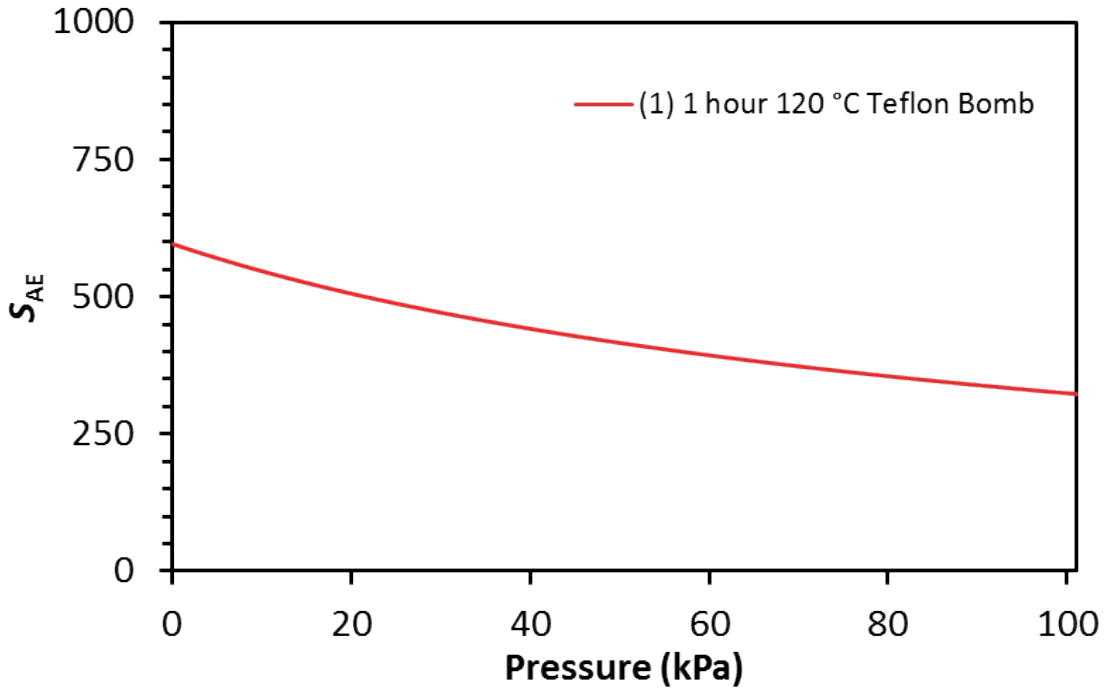


**Figure S3.15.** IAST selectivity calculation for a 1:99 $C_2H_2/C_2H_4$ gas mixture adsorbed onto the **SIFSIX-14-Cu-i** sample obtained from a Parr® teflon bomb after heating at 120 °C for 1 hour.

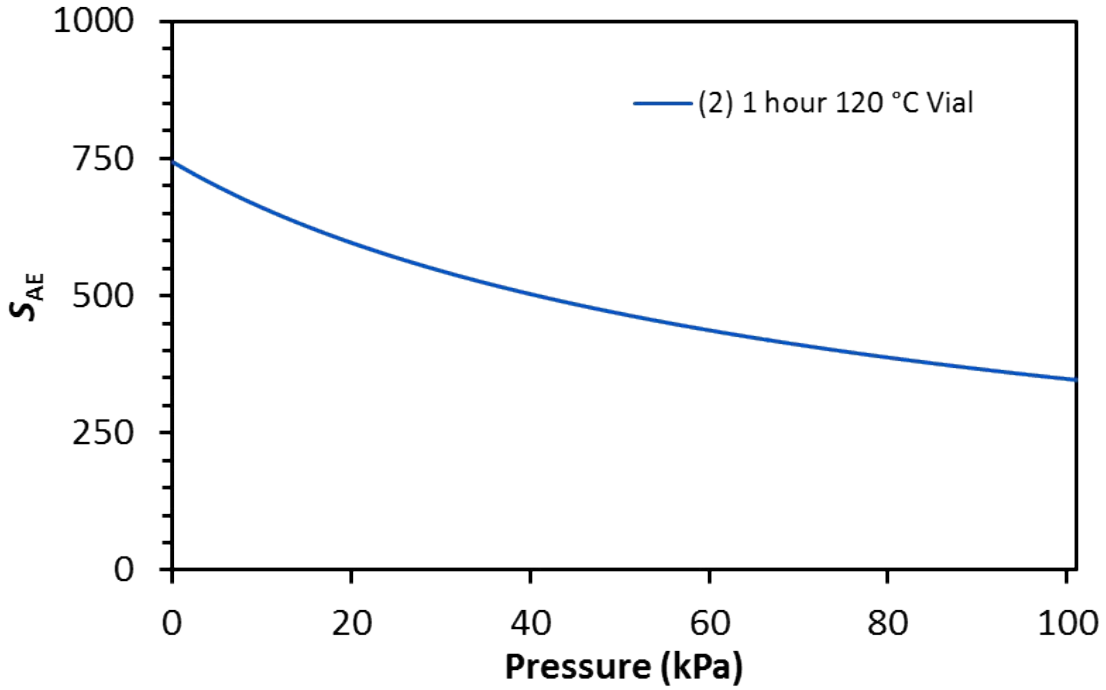


**Figure S3.16.** IAST selectivity calculation for a 1:99 $C_2H_2/C_2H_4$ gas mixture adsorbed onto the **SIFSIX-14-Cu-i** sample obtained from a Schott® bottle after heating at 120 °C for 1 hour.

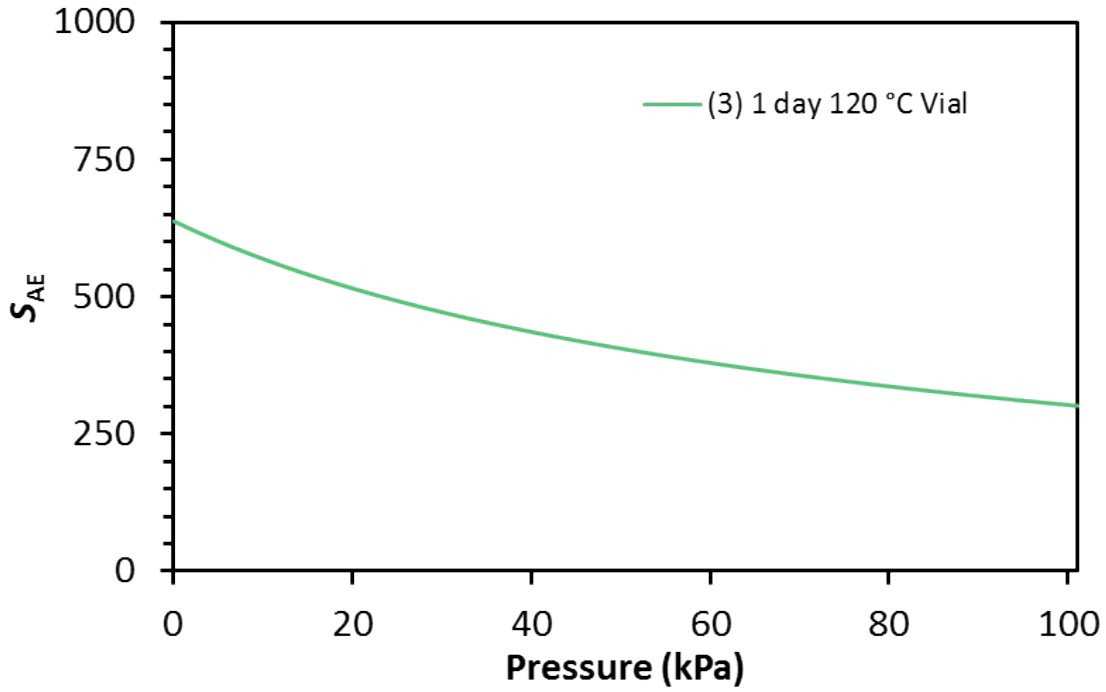


**Figure S3.17.** IAST selectivity calculation for a 1:99 $C_2H_2/C_2H_4$ gas mixture adsorbed onto **the SIFSIX-14-Cu-i** sample obtained from a Schott® bottle after heating at 120 °C for 1 day.

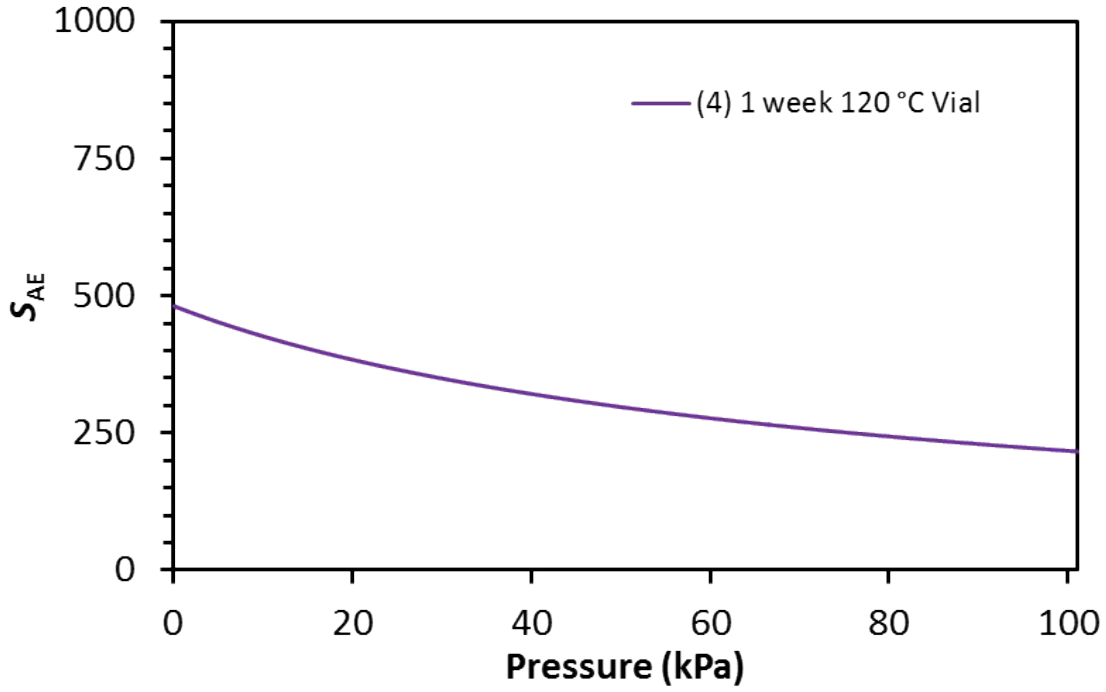


**Figure S3.18.** IAST selectivity calculation for a 1:99 $C_2H_2/C_2H_4$ gas mixture adsorbed onto the **SIFSIX-14-Cu-i** sample obtained from a Schott® bottle after heating at 120 °C for 1 week.

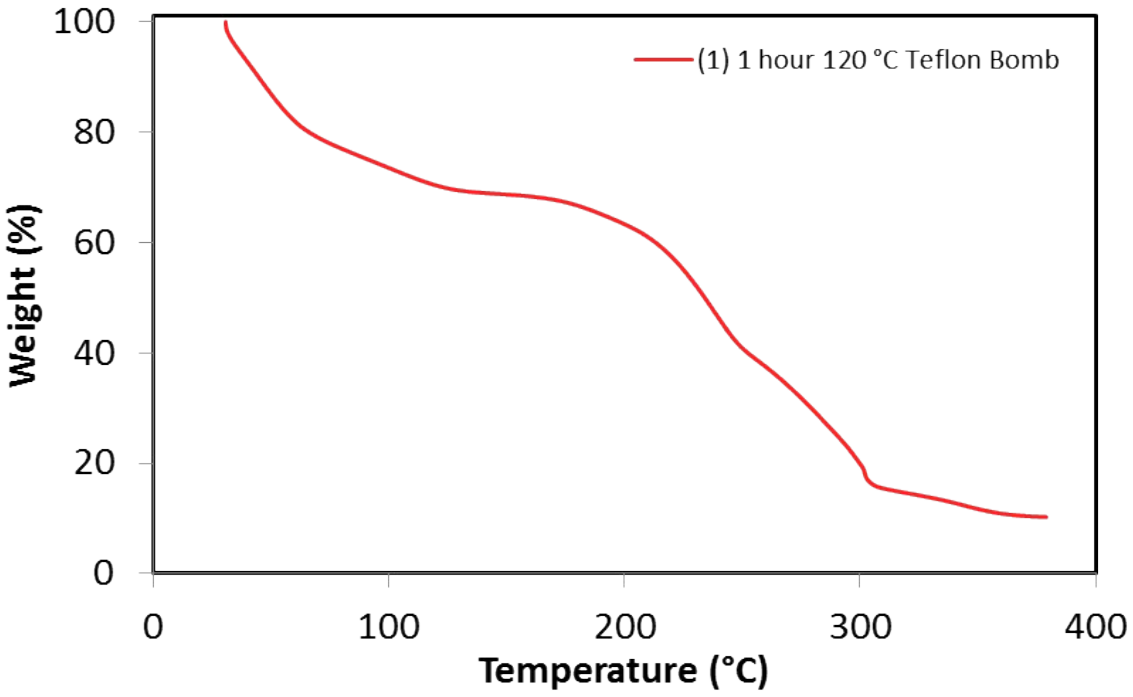


**Figure S3.19.** Thermogravimetric trace of the **SIFSIX-14-Cu-i** sample obtained from a Parr® teflon bomb after heating at 120 °C for 1 hour.

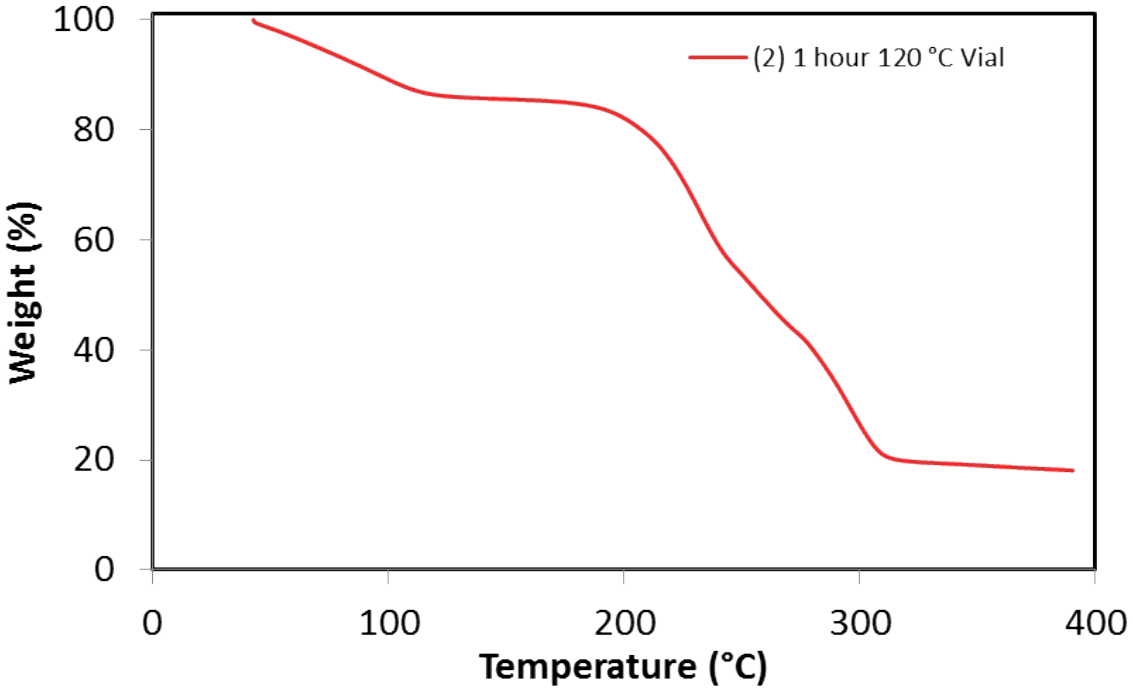


**Figure S3.20.** Thermogravimetric trace of the **SIFSIX-14-Cu-i** sample obtained from a Schott® teflon bomb after heating at 120 °C for 1 hour.

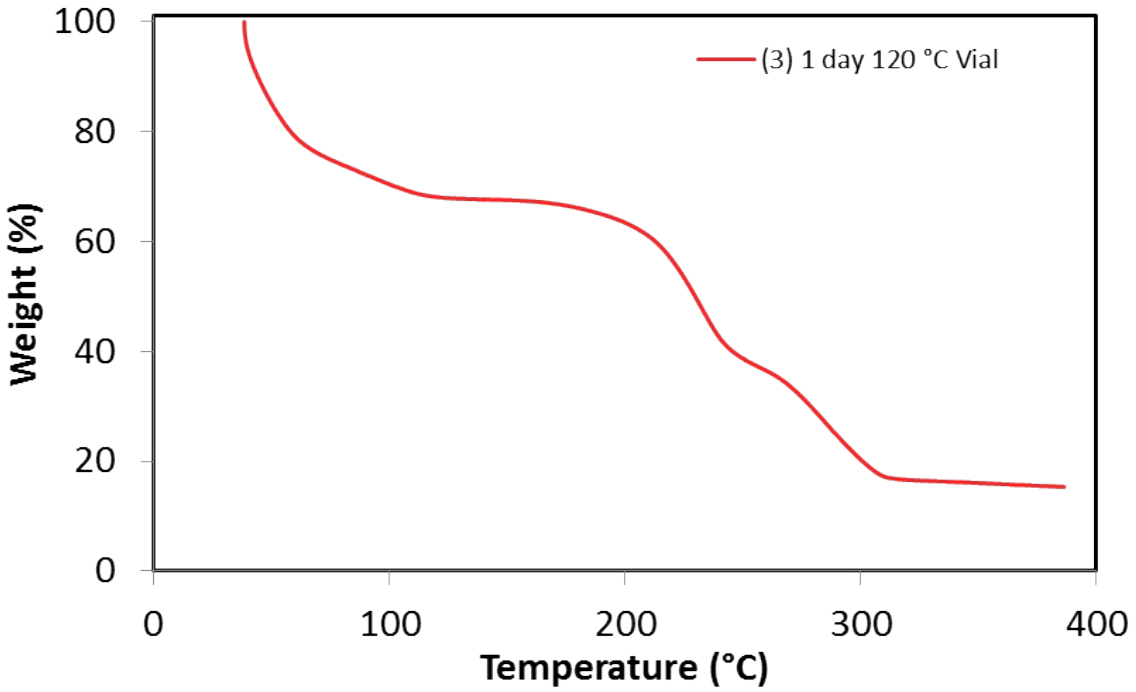


**Figure S3.21.** Thermogravimetric trace of the **SIFSIX-14-Cu-i** sample obtained from a Schott® bottle after heating at 120 °C for 1 day.

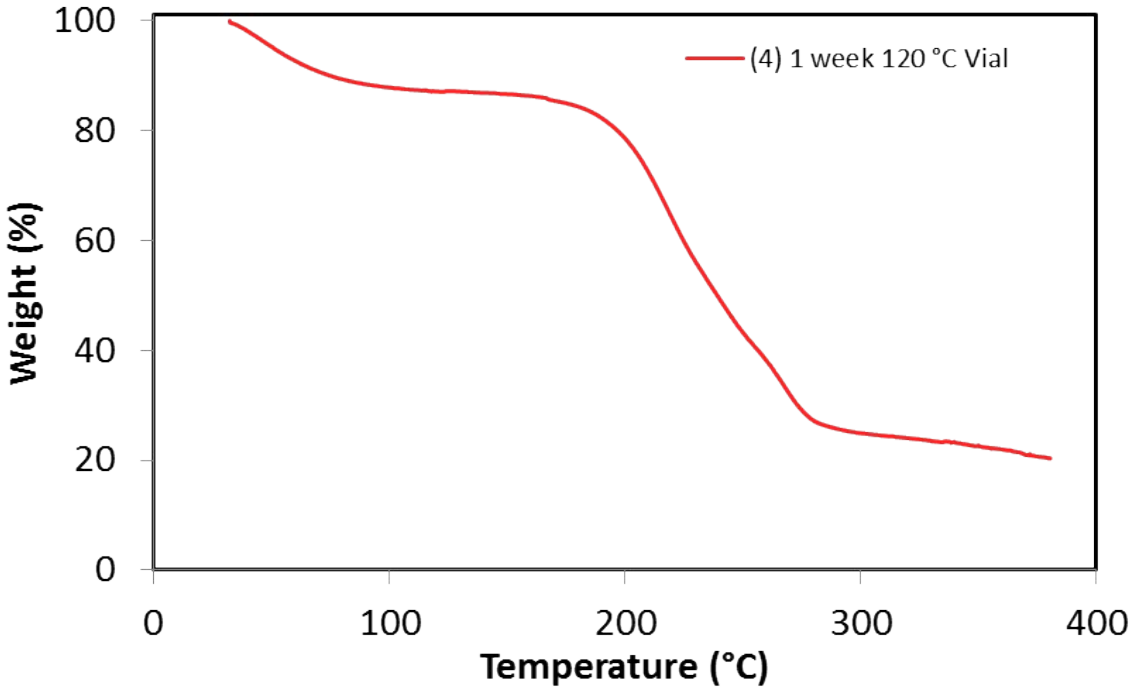


**Figure S3.22.** Thermogravimetric trace of the **SIFSIX-14-Cu-i** sample obtained from a Schott® bottle after heating at 120 °C for 1 week.

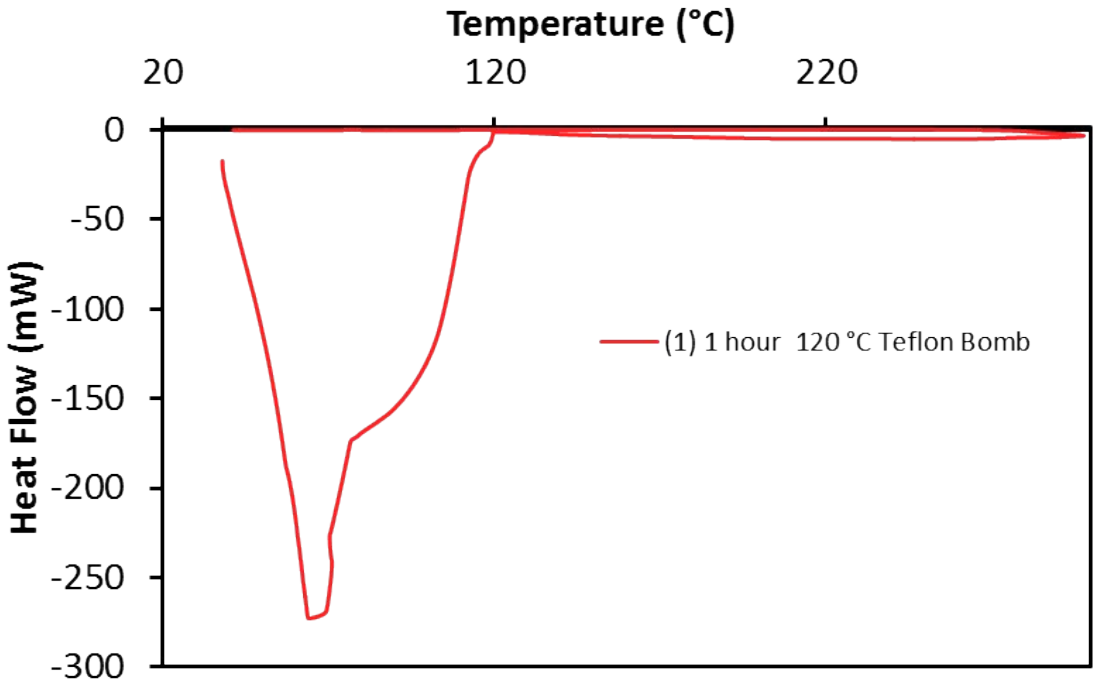


**Figure S3.23.** Differential scanning calorimetry trace of the **SIFSIX-14-Cu-i** sample obtained from a Parr® teflon bomb after heating at 120 °C for 1 hour.

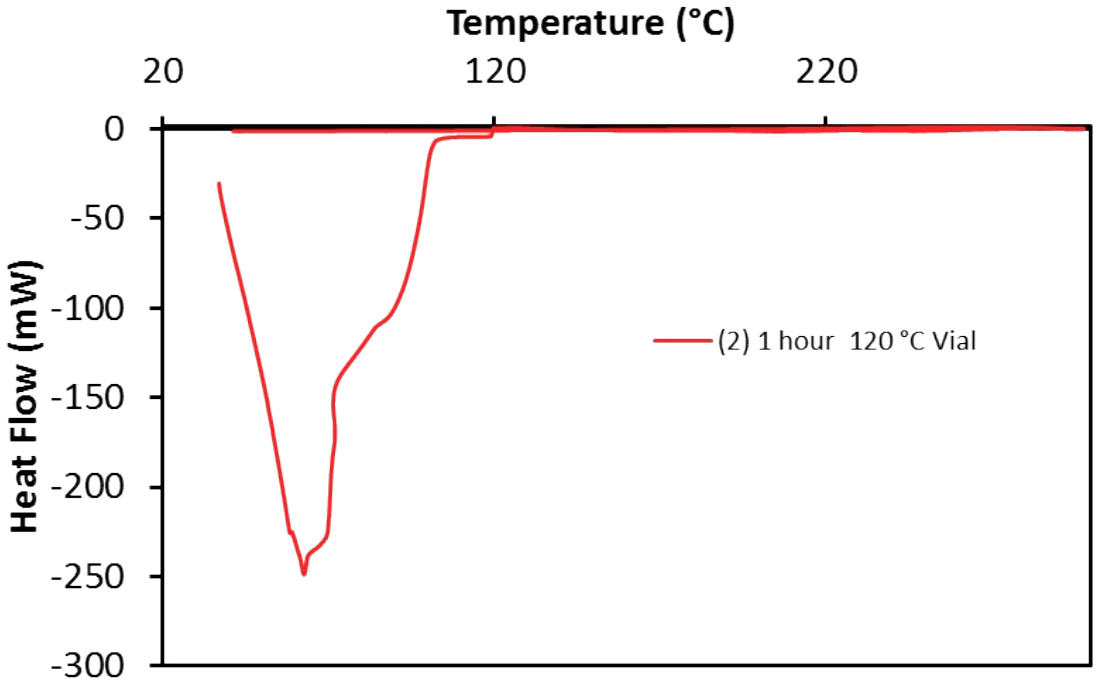


**Figure S3.24.** Differential scanning calorimetry trace of the **SIFSIX-14-Cu-i** sample obtained from a Schott® bottle after heating at 120 °C for 1 hour.

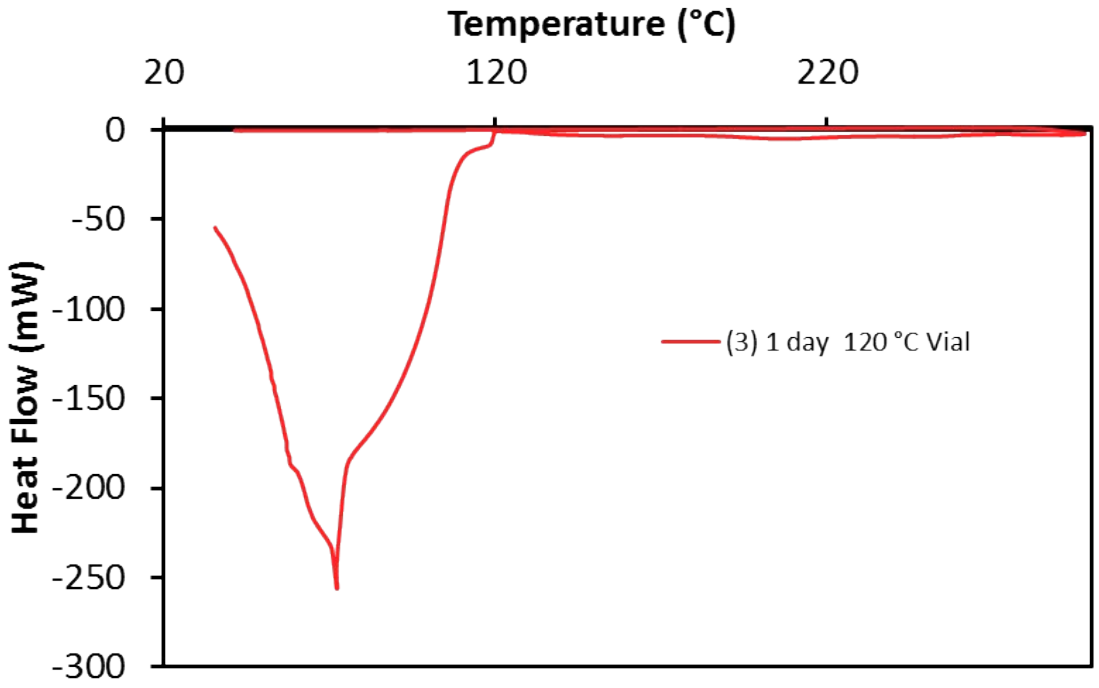


**Figure S3.25.** Differential scanning calorimetry trace of the **SIFSIX-14-Cu-i** sample obtained from a Schott® bottle after heating at 120 °C for 1 day.

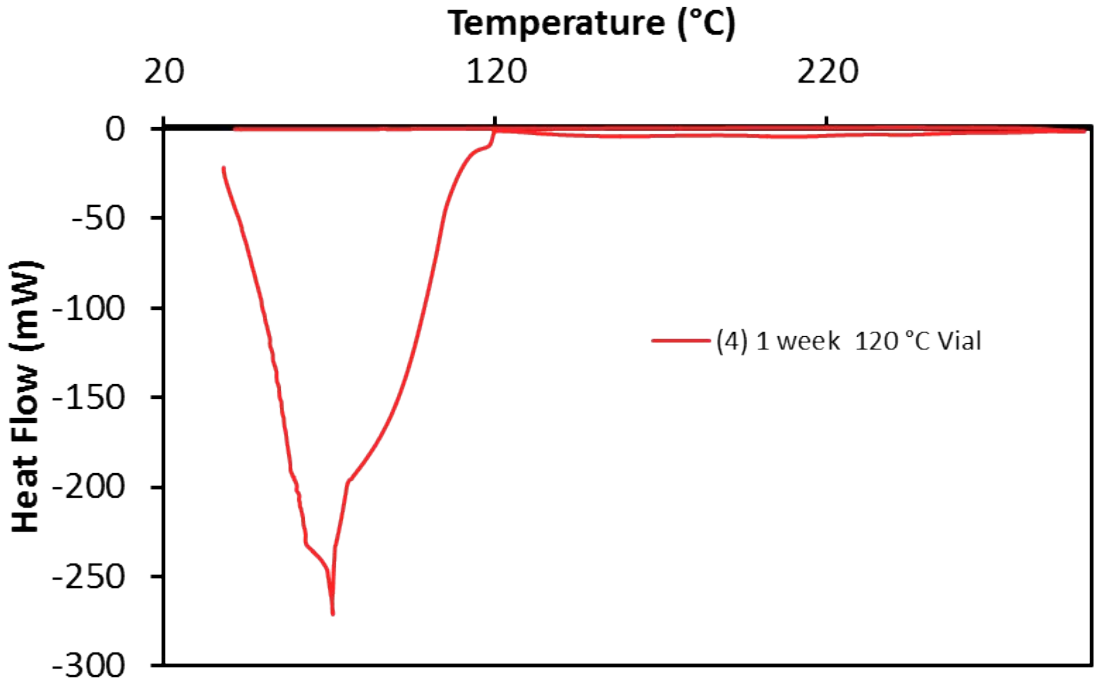


**Figure S3.26.** Differential scanning calorimetry trace of the **SIFSIX-14-Cu-i** sample obtained from a Schott® bottle after heating at 120 °C for 1 week.

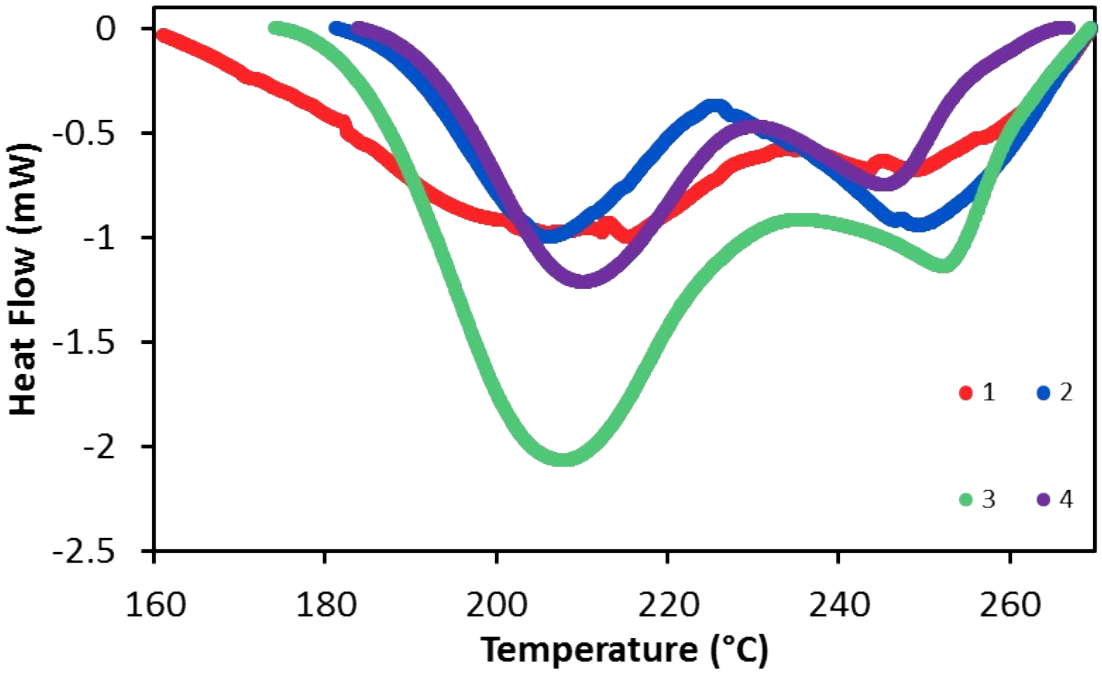


**Figure S3.27.** Baseline-corrected differential scanning calorimetry traces of all compounds reported herein, between the temperatures where decomposition occurs.

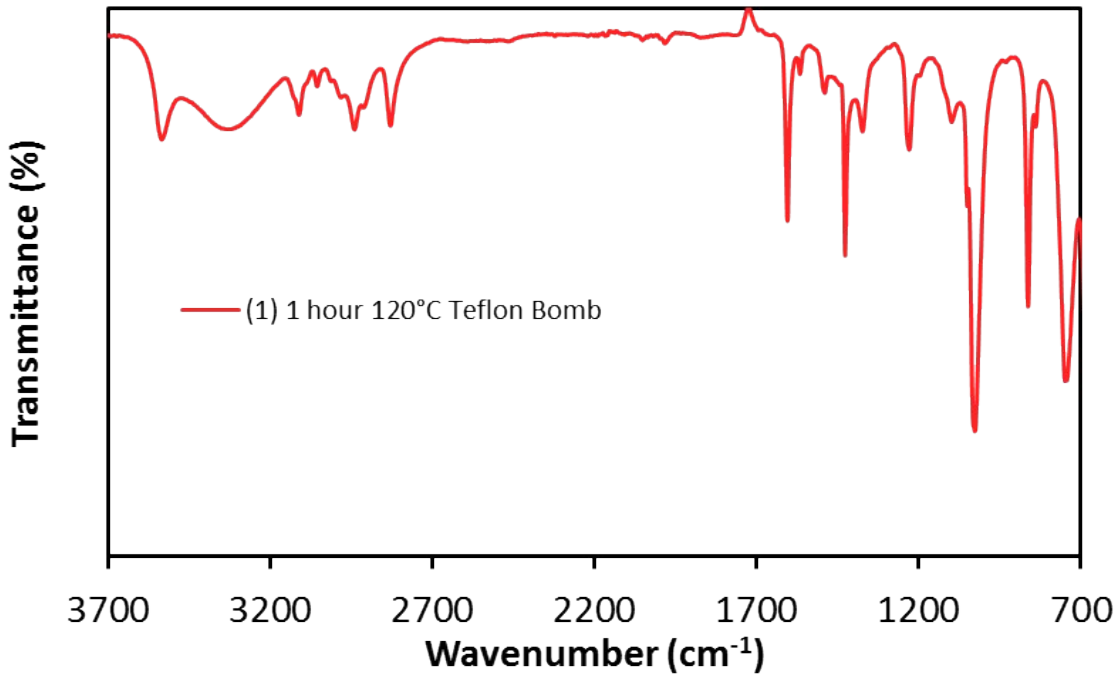


Figure S3.28. ATR-FT-IR spectra of the **SIFSIX-14-Cu-i** sample obtained from a Parr® teflon bomb after heating at 120 °C for 1 hour.

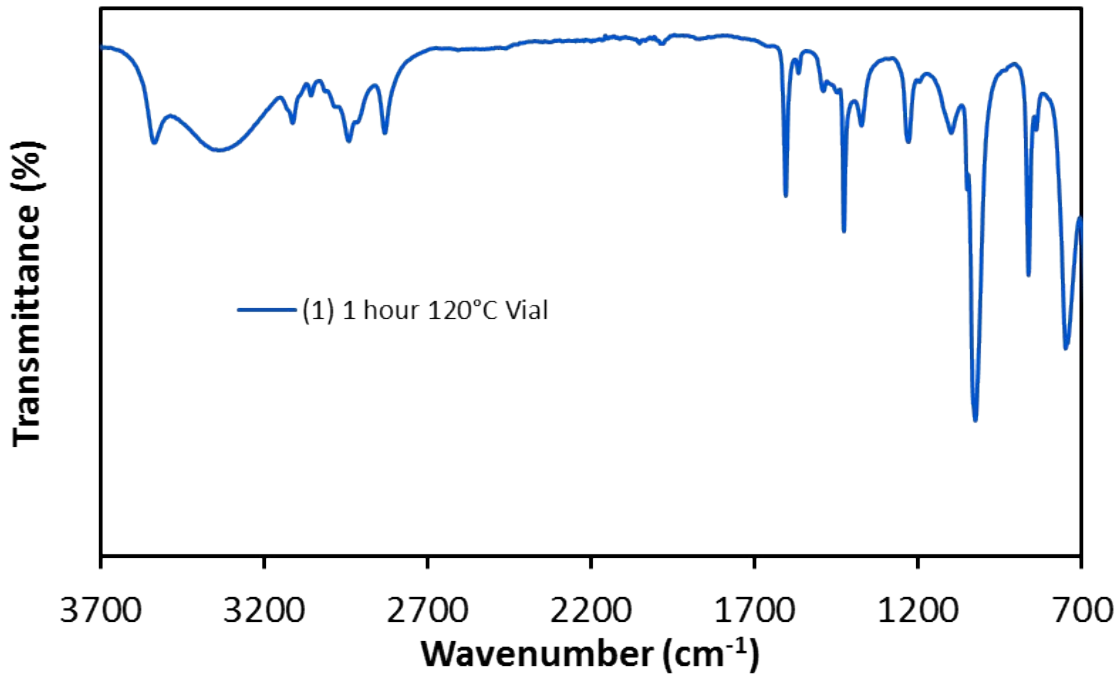


**Figure S3.29.** ATR-FT-IR spectra of the **SIFSIX-14-Cu-i** sample obtained from a Schott® bottle after heating at 120 °C for 1 hour.

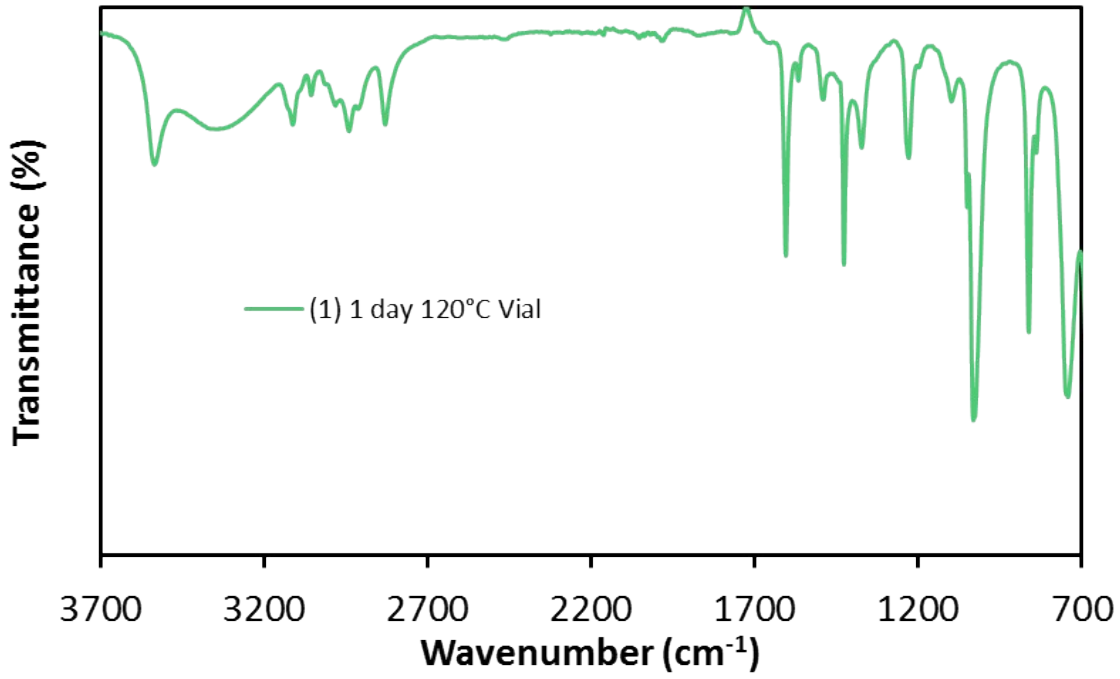


**Figure S3.30.** ATR-FT-IR spectra of the **SIFSIX-14-Cu-i** sample obtained from a Schott® bottle after heating at 120 °C for 1 day.

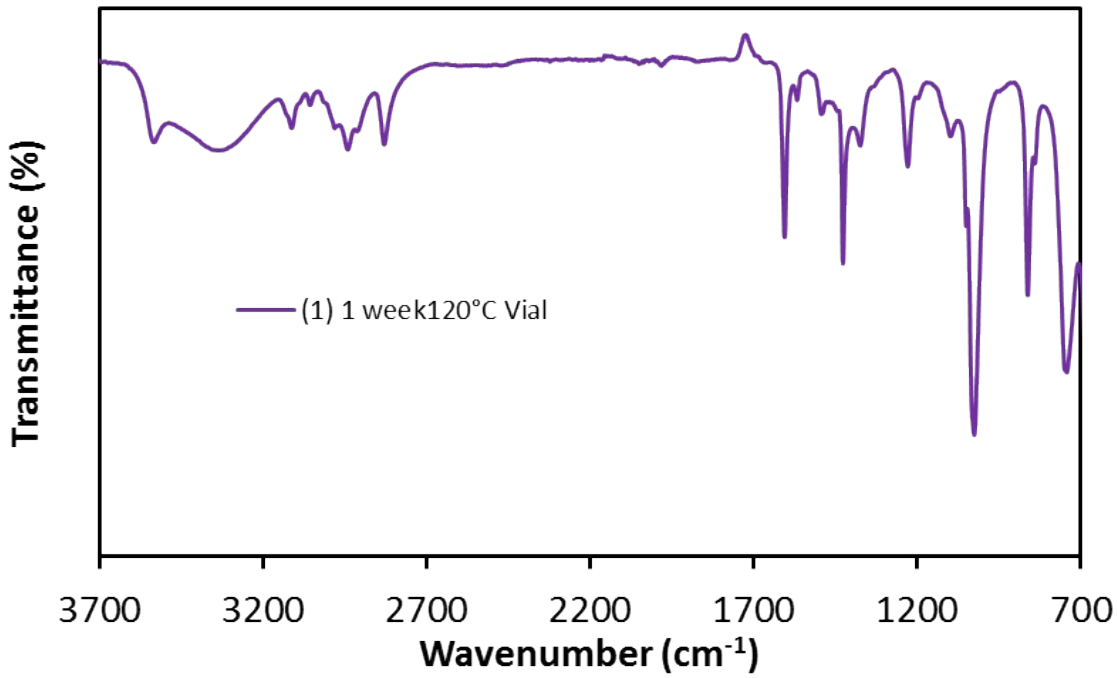


**Figure S3.31.** ATR-FT-IR spectra of the **SIFSIX-14-Cu-i** sample obtained from a Schott® bottle after heating at 120 °C for 1 week.

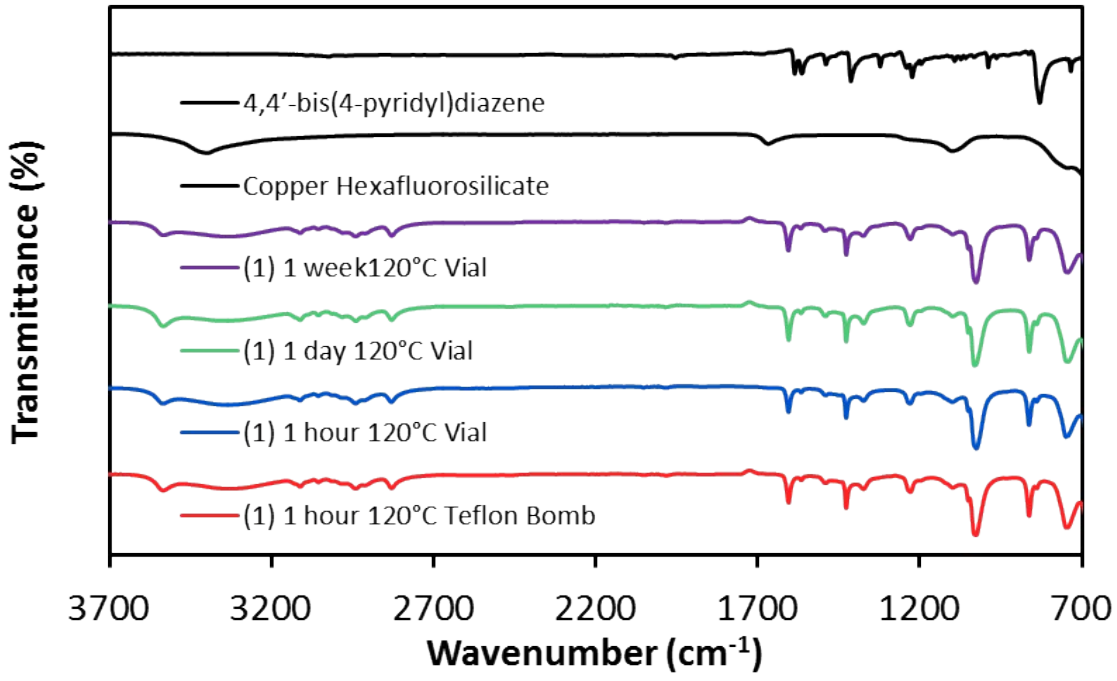


**Figure S3.32.** ATR-FT-IR spectra of all compounds reported herein.

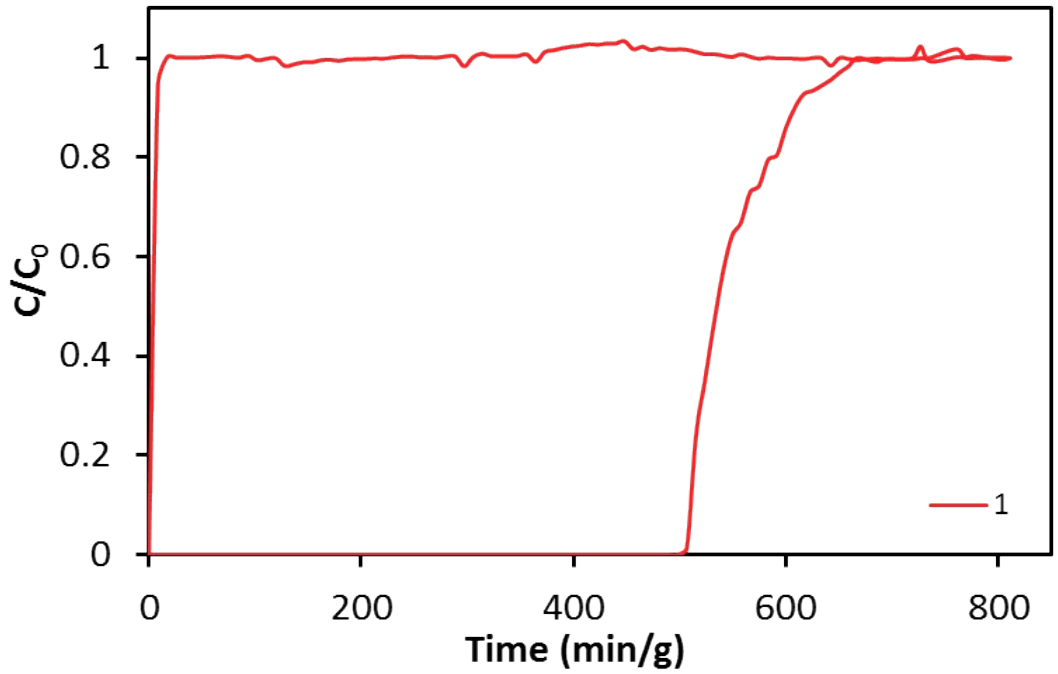


**Figure S3.33.** Dynamic breakthrough of a 1:99 $C_2H_2/C_2H_4$ gas mixture (5 ml/min) of the **SIFSIX-14-Cu-i** sample obtained from a Parr® teflon bomb after heating at 120 °C for 1 hour.

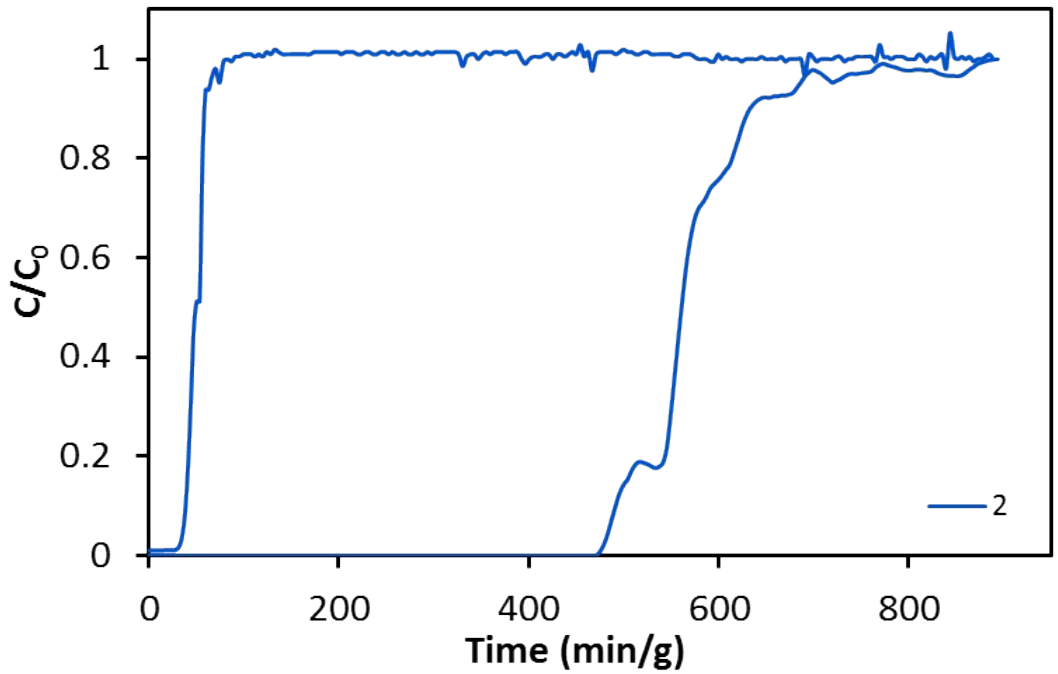


**Figure S3.34.** Dynamic breakthrough of a 1:99 $C_2H_2/C_2H_4$ gas mixture (5 ml/min) of the **SIFSIX-14-Cu-i** sample obtained from a Schott® bottle after heating at 120 °C for 1 hour.

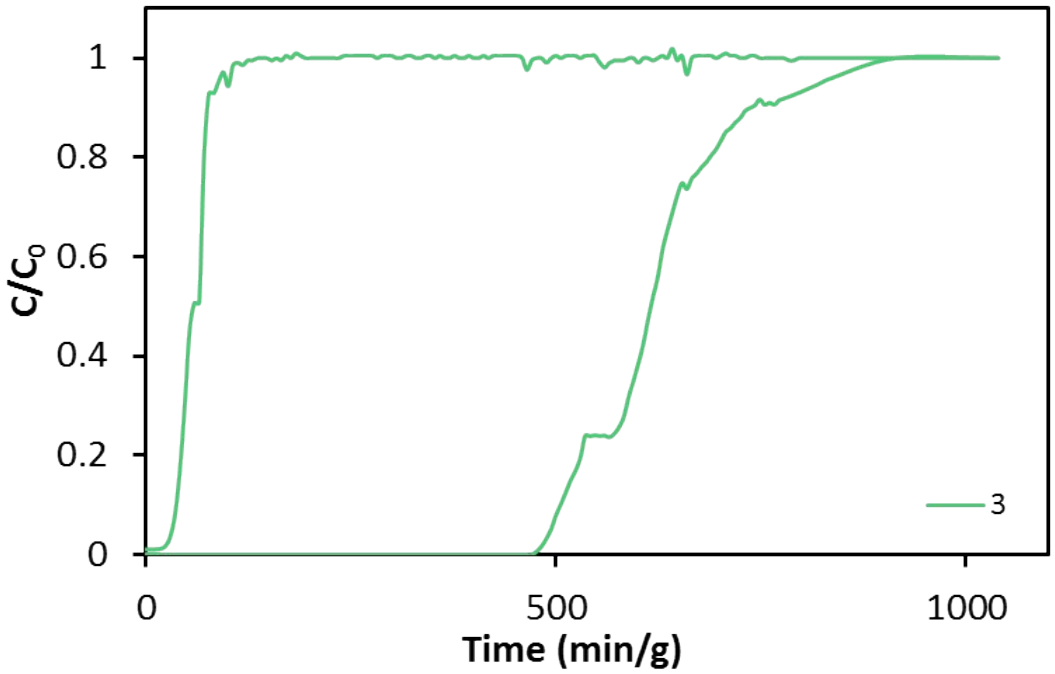


**Figure S3.35.** Dynamic breakthrough of a 1:99 $C_2H_2/C_2H_4$ gas mixture (5 ml/min) of the **SIFSIX-14-Cu-i** sample obtained from a Schott® bottle after heating at 120 °C for 1 day.

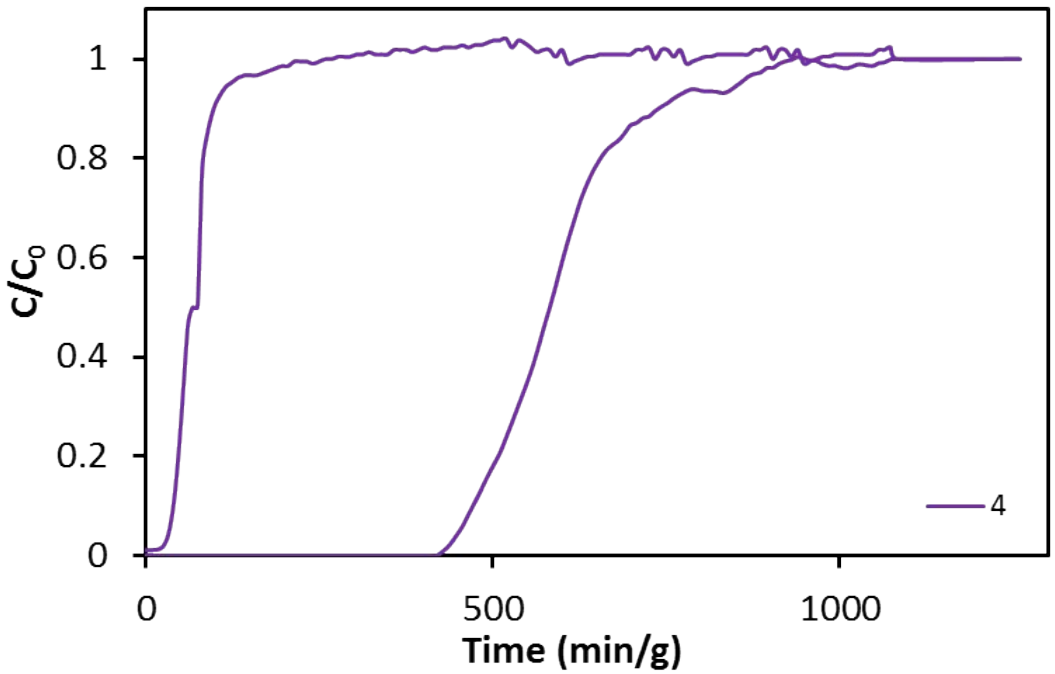


**Figure S3.36.** Dynamic breakthrough of a 1:99 $C_2H_2/C_2H_4$ gas mixture (5 ml/min) of the **SIFSIX-14-Cu-i** sample obtained from a Schott® bottle after heating at 120 °C for 1 week.

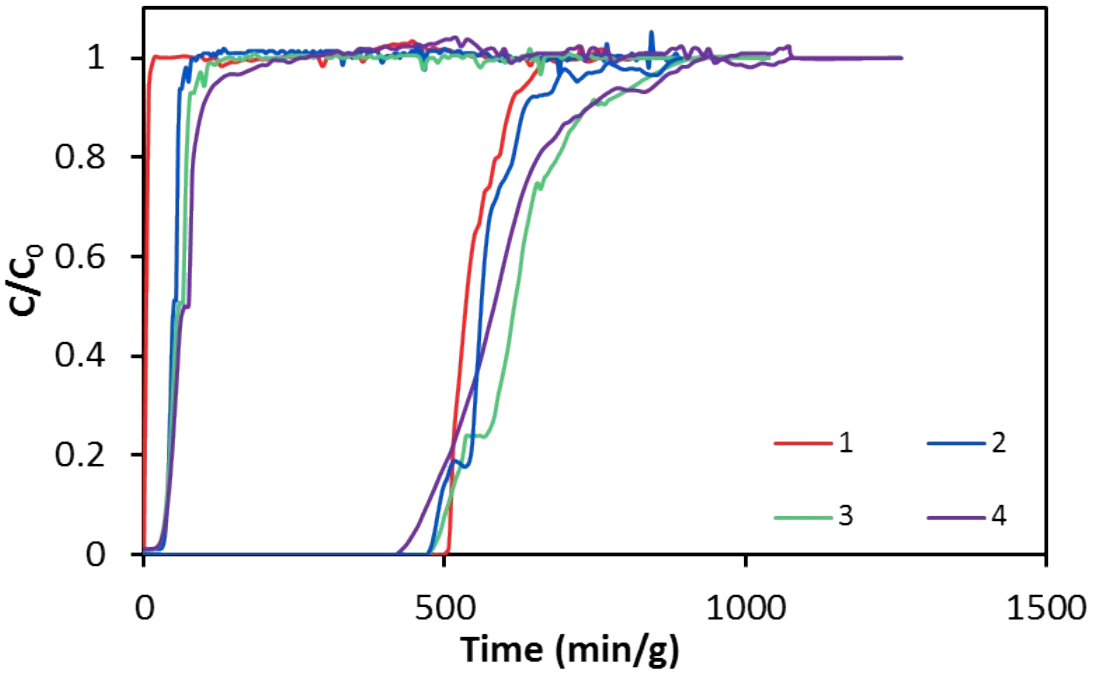


**Figure S3.37.** Dynamic breakthrough of a 1:99 $C_2H_2/C_2H_4$ gas mixture (5 ml/min) of all samples reported herein.

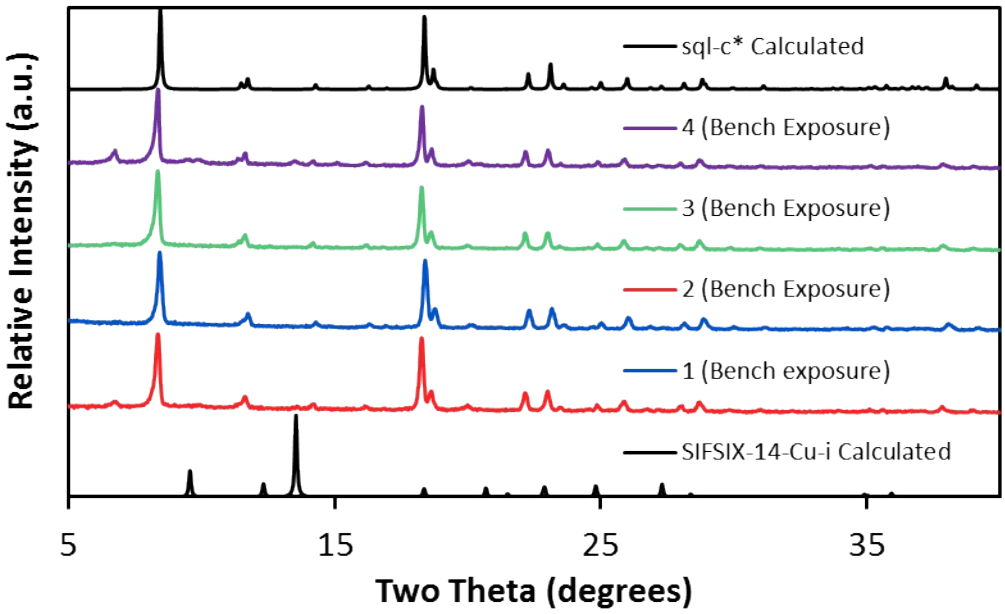


**Figure S3.38.** Laboratory X-ray powder diffractograms of all samples reported herein after 24 h of benchtop exposure to ambient temperature/pressure/humidity, indicating phase transformation to the **sql-c*** network topology.

**Molecular Modelling**

The single X-ray crystallographic structure of **SIFSIX-14-Cu-i** that was published in reference 1 was used for the parametrizations and simulations in this work. A non-interpenetrated version of **SIFSIX-14-Cu-i** was used as the structural model for **SIFSIX-14-Cu**. Simulations of $N_2$ adsorption in both HUMs were performed using grand canonical Monte Carlo (GCMC) methods[5] in a 3 × 1 × 1 supercell. A spherical cut-off distance of 9.23815 Å was used for the simulations; this value corresponds to half the shortest supercell dimension length. $N_2$ was modeled using a rigid five-site electrostatic (nonpolarizable) potential that was developed previously.[6] The parameters for this model are provided in **Table S3.3**.

The total potential energy of the HUM–$N_2$ system was calculated through the sum of the repulsion/dispersion and stationary electrostatic energies. These were calculated using the Lennard-Jones 12–6 potential[7] and partial charges with Ewald summation,[8] respectively. For the former, the interactions between unlike species were governed by the Lorentz-Bertholet mixing rules.[9] Note, the main goal for the modeling studies in this work was to obtain a saturated loading amount for $N_2$ in **SIFSIX-14-Cu** and **SIFSIX-14-Cu-i**. Therefore, we believe that utilizing nonpolarizable potentials for the HUMs and adsorbate were sufficient for this study, especially considering the dramatic increase in computational speed relative to simulations involving classical polarization. Nevertheless, we expect that simulations including explicit many-body polarization interactions[10] will produce the same saturation structures that were obtained herein by the nonpolarizable force field. The chemical potential for $N_2$ was determined through the Peng–Robinson equation of state.[11] Simulations of $N_2$ adsorption in both HUMs were carried out at 77 K and 1 atm with all HUM atoms held fixed at their crystallographic positions. All

simulations were performed using the Massively Parallel Monte Carlo (MPMC) code, an open-source code that is currently available for download on GitHub.[12]

The Lennard-Jones 12–6 parameters (ε and σ) for all C, H, and N atoms were taken from the Optimized Potentials For Liquid Simulations – All Atom (OPLS-AA) force field,[13] while such parameters for the F, Si, and Cu atoms were taken from the Universal Force Field (UFF).[14] The crystal structure of **SIFSIX-14-Cu-i** contains 30 atoms in chemically distinct environments (**Figures S3.39**). The partial charges for each unique atom in **SIFSIX-14-Cu-i** were determined through electronic structure calculations on different gas phase fragments that were selected from the crystal structure of the HUM. For these calculations, all C, H, N, F, and Si atoms were treated with the 6-31G* basis set, while the LANL2DZ ECP basis set[15] was used for the $Cu^{2+}$ ions. The NWChem *ab initio* software package[16] was used to calculate the electrostatic potential surface for each fragment and the partial charges were subsequently fitted onto the atomic positions of the fragments using the CHELPG method.[17] For each chemically distinct atom, the partial charges were averaged between the fragments. The partial charges were then adjusted so that the total charge of the system was equal to zero. The resulting partial charges for each chemically distinguishable atom in **SIFSIX-14-Cu-i** are provided in **Table S3.4**. Note, since the structural model used herein for **SIFSIX-14-Cu** was derived from the crystal structure of **SIFSIX-14-Cu-i**, simulations in the former employed the same partial charges for the unique atoms as its doubly interpenetrated polymorph. The modeled 3 × 1 × 1 supercells of **SIFSIX-14-Cu** and **SIFSIX-14-Cu-i** at $N_2$ saturation are shown in **Figures S40** and **S41**, respectively.

**Table S3.3.** Parameters for the five-site electrostatic potential for $N_2$ that was used for the simulations in this work. *r* corresponds to the distance from the center-of-mass (COM) and OS refers to the phantom site associated with the model.

| Site | *r* (Å) | ε (K) | σ (Å) | *q* ($e^-$) |
|---|---|---|---|---|
| **COM** | 0.000 | 17.60293 | 3.44522 | +1.04742 |
| **N** | 0.549 | 0.00000 | 0.00000 | –0.52371 |
| **OS** | 0.738 | 18.12772 | 3.15125 | 0.00000 |

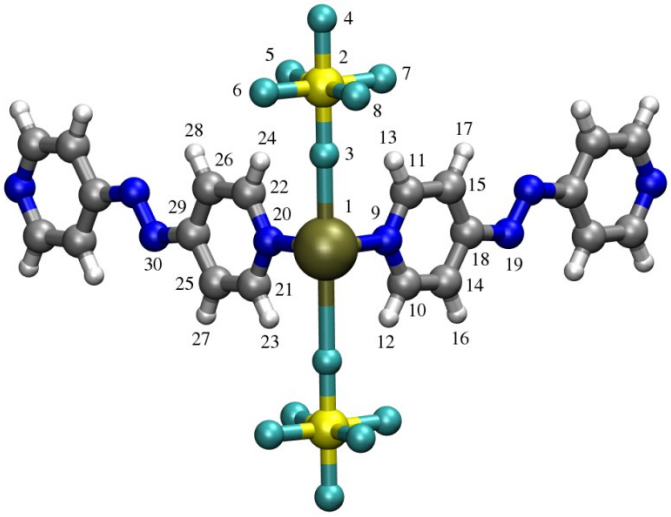


**Figure S3.39**. The numbering of the chemically distinct atoms in **SIFSIX-14-Cu** and **SIFSIX-14-Cu-i** as referred to in **Table S2**. Atom colors: C = gray, H = white, N = blue, F = cyan, Si = yellow, Cu = gold.

**Table S3.4.** The partial charges (in $e^-$) for the chemically distinct atoms in **SIFSIX-14-Cu** and **SIFSIX-14-Cu-i** that were used for the simulations in this work. Label of atoms correspond to **Figure S1**.

| **Atom** | **Label** | ***q*** **($e^-$)** |
|---|---|---|
| Cu | 1 | 0.4159 |
| Si | 2 | 1.7826 |
| F | 3 | –0.6255 |
| F | 4 | –0.6239 |
| F | 5 | –0.6152 |
| F | 6 | –0.6205 |
| F | 7 | –0.6215 |
| F | 8 | –0.6303 |
| N | 9 | –0.3417 |
| C | 10 | 0.3161 |
| C | 11 | 0.2413 |
| H | 12 | 0.1639 |
| H | 13 | 0.1701 |
| C | 14 | –0.4882 |
| C | 15 | –0.4257 |
| H | 16 | 0.2112 |
| H | 17 | 0.1734 |
| C | 18 | 0.5777 |
| N | 19 | –0.2061 |
| N | 20 | –0.3100 |
| C | 21 | 0.2736 |
| C | 22 | 0.2088 |
| H | 23 | 0.1693 |
| H | 24 | 0.1771 |
| C | 25 | –0.4541 |
| C | 26 | –0.4153 |
| H | 27 | 0.2029 |
| H | 28 | 0.1643 |
| C | 29 | 0.5579 |
| N | 30 | –0.1973 |

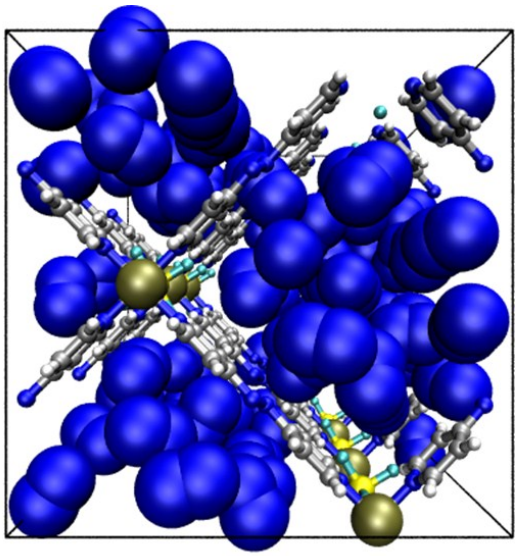

(a)

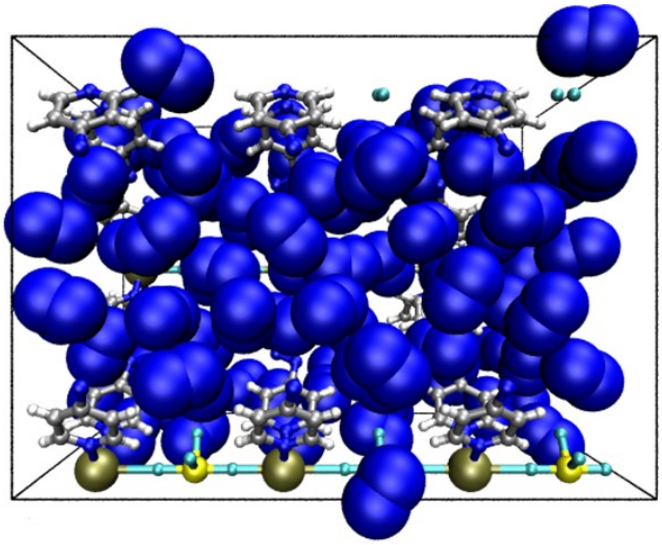

(b)

**Figure S3.40**. (a) *a*-axis view and (b) *c*-axis view of the modeled 3 × 1 × 1 supercell of **SIFSIX-14-Cu** at $N_2$ saturation, which corresponds to 33 molecules per unit cell (or 28.71 mmol $g^{-1}$). Atom colors: C = gray, H = white, N = blue, F = cyan, Si = yellow, Cu = gold.

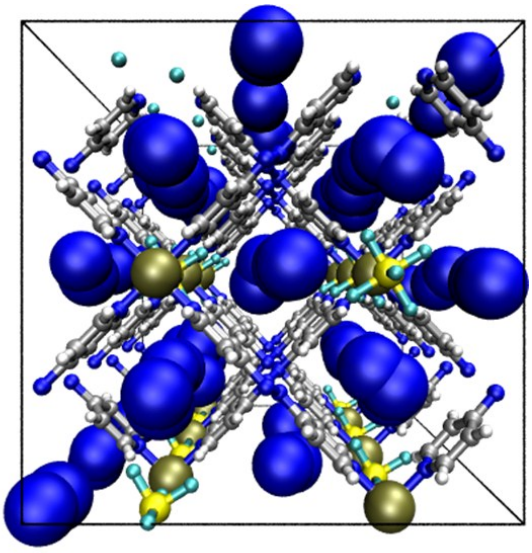

(a)

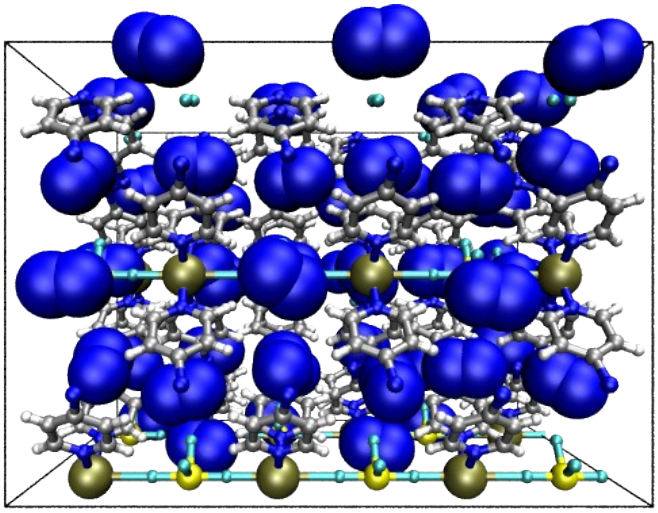

(b)

**Figure S3.41.** (a) *a*-axis view and (b) *c*-axis view of the modeled 3 × 1 × 1 supercell of **SIFSIX-14-Cu-i** at $N_2$ saturation, which corresponds to 16 molecules per unit cell (or 6.97 mmol $g^{-1}$). Atom colors: C = gray, H = white, N = blue, F = cyan, Si = yellow, Cu = gold.

**References**


1. O'Nolan, D.; Kumar, A.; Zaworotko, M. J. *J. Am. Chem. Soc*. 2017, **139**, 8508–8513.

2. Myers, A. L.; Prausnitz, J. M. *AIChE J.* 1965, **11**, 121.

3. Simon, C. M.; Smit, B.; Haranczyk, M. *Comp. Phys. Commun.* 2016, **200**, 364-380.

4. Simon, C. M. "PyIAST". https://github.com/CorySimon/pyIAST (accessed Oct 11, 2017).

5. 2.) Metropolis, N.; Rosenbluth, A. W.; Rosenbluth, M. N.; Teller, A. H.; Teller, E. *J. Chem. Phys.* 1953, **21**, 1087–1092.

6. Cioce, C. R.; McLaughlin, K.; Belof, J. L.; Space, B. *J. Chem. Theory Comput*. 2013, **9**, 5550−5557.

7. Jones, J. E. *Proc. R. Soc. A* 1924, **106**, 463–477.

8. (a) Ewald, P. P.; *Ann. Phys*. 1921, **369**, 253–287.

   (b) Wells, B. A.; Chaffee, A. L. *J. Chem. Theory Comput*. 2015, **11**, 3684–3695.

9. Allen, M. P.; Tildesley, D. J. *Computer Simulations of Liquids*; Oxford University Press: Oxford, United Kingdom, 1989; pp. 21.

10. (a) Applequist, J.; Carl, J. R.; Fung, K.-K. *J. Am. Chem. Soc*. 1972, **94**, 2952−2960.

    (b) Thole, B. *Chem. Phys*. 1981, **59**, 341−350.

    (c) Bode, K. A.; Applequist, J. *J. Phys. Chem*. 1996, **100**, 17820−17824.

(d) McLaughlin, K.; Cioce, C. R.; Pham, T.; Belof, J. L.; Space, B. *J. Chem. Phys*. 2013, **139**, 184112.

11. Peng, D.-Y.; Robinson, D. B. *Ind. Eng. Chem. Fundam*. 1976, **15**, 59–64.

12. Belof, J. L.; Space, B. *Massively Parallel Monte Carlo (MPMC)*. 2012, Available on GitHub. https://github.com/mpmccode/mpmc.

13. Jorgensen, W. L.; Maxwell, D. S.; Tirado-Rives, J. *J. Am. Chem. Soc*. 1996, **118**, 11225–11236.

14. Rappé, A. K.; Casewit, C. J.; Colwell, K. S.; Goddard, W. A.; Skiff, W. M. *J. Am. Chem. Soc*. 1992, **114**, 10024–10035.

15. (a) Stevens, W. J.; Basch, H.; Krauss, M. *J. Chem. Phys*. 1984, **81**, 6026–6033.

(b) Hay, P. J.; Wadt, W. R. *J. Chem. Phys*. 1985, **82**, 270–283.

(c) LaJohn, L. A.; Christiansen, P. A.; Ross, R. B.; Atashroo, T.; Ermler, W. C. *J. Chem. Phys*. 1987, **87**, 2812–2824.

16. Valiev, M.; Bylaska, E.; Govind, N.; Kowalski, K.; Straatsma, T.; Dam, H. V.; Wang, D.; Nieplocha, J.; Apra, E.; Windus, T.; de Jong, W. *Comput. Phys. Commun*. 2010, **181**, 1477–1489.

17. (a) Chirlian, L. E.; Francl, M. M. *J. Comput. Chem*. 1987, 8, 894–905.

(b) Breneman, C. M.; Wiberg, K. B. *J. Comput. Chem*. 1990, **11**, 361–373.